

Finely Grained PbTe and BiSbTe for Low Thermal
Conductivity and High ZT values

(低熱伝導率と高 ZT のための微細結晶粒テルル化鉛と
テルル化ビスマスアンチモン)

Mongkol Bumrungpon

Graduate School of Advanced Technology and Science
Intelligent Structures and Mechanics Systems Engineering
Mechanical Engineering
Tokushima University
September 2020

CONTENTS

CHAPTER	Page
1. INTRODUCTION	3
1.1 Background and history of thermoelectric	
1.2 Performance evaluation of thermoelectric materials	
1.3 Lead telluride properties and literature review	
1.4 Bismuth antimony telluride properties and literature review	
1.5 Research objectives	
2. EXPERIMENTATION AND METHODOLOGY	17
2.1 PbTe materials and preparation methods	
2.2 BiSbTe materials and preparation methods	
2.3 X-ray diffraction	
2.4 Microstructures, grain sizes and EDS	
2.5 Electrical conductivity	
2.6 Seebeck coefficient	
2.7 Thermal conductivity	
2.8 Dimensionless figure of merit ZT	
3. RESULTS AND DISCUSSION	24
3.1 PbTe results and discussion	
3.2 BiSbTe results and discussion	
4. CONCLUSIONS	54
4.1 Lead telluride (PbTe) research conclusions	
4.2 Bismuth antimony telluride (BiSbTe) research conclusions	

REFERENCES	57
LIST OF PUBLICATIONS	66

CHAPTER 1

INTRODUCTION

1.1 Background and history of thermoelectric

In 1821, T. J. Seebeck discovered the first thermoelectric effect. Electromotive force can be produced by heating the junction, between two kinds of different electrical conductors. Then, it can be demonstrated by connecting two wires made of different metals. The ends of the wires which are not touching are then connected to the terminals of a galvanometer. When the junction between the wires is heating, the meter can record a small voltage. The magnitude of thermoelectric voltage is equal to the difference of temperature recorded at the thermocouple junction, and the temperature recorded at the connections to the galvanometer.

Thirteen years after Thomas Johann Seebeck found this experiment, Jean Charles Athanase Peltier discovered the second thermoelectric effect. The moving direction of the electric current through a thermocouple produces small cooling or heating effect, it depends on moving direction. Since this ideal is always accompanied by the Joule heating effect, it is quite difficult to demonstrate by using metallic thermocouples. Sometimes, the only thing one can show is that there is less heating during the current passing in one way than there is when it passes in the other. The arrangement can however be used to demonstrate the Peltier effect if the meter is replaced with a direct current source, and a small thermometer is placed on the thermocouple junction.

Peltier and Seebeck effects are correlated. However, this interdependency was recognized by William Thomson in 1855. The theory of thermodynamics was applied to the problem by Thomson, for the relationship between the coefficients that describe the Peltier and Seebeck effects. Peltier and Seebeck effects happen only at junctions among

different conductors, suggesting that they are interfacial phenomena. However, they depend on the properties of conductor materials. Presently, it is understood that electric current is carried through a conductor by means of electrons, that can possess different kinds of energy levels depending on the material. When a current pass from one material to another, the energy transported by the electrons is altered. This alteration is reflected in the heating or the cooling of the junction, which is the Peltier effect. Also, when the temperature at the junction increases, electrons are enabled to pass from materials in which they have lower energy levels to materials in which they have higher energy levels, causing electromotive force [1].

Thomson effect shows how a thermocouple is a type of heat engine. It can be applied for generating electricity from heat or, on the other hand, applied to use as a refrigerator. So, this reversible effect is always accompanied by the irreversible phenomena of Joule heating and thermal conduction. Then, thermocouples tend to be inefficient. In 1911, Altenkirch analyzed a problem of energy conversion by using thermocouples. This idea showed how a thermocouple can be more improved. The ways to improve, that is, increase the magnitude of the differential Seebeck coefficient and increase the electrical conductivity of the two components, and try to reduce the total thermal conductivity. Albeit the Seebeck effect has been used for the detection of thermal radiation and for the measurement of temperature, at the time no thermocouples with the right combination of properties for efficient energy conversion existed.

In 1950, the semiconductor was introduced as thermoelectric materials, that an applied Peltier refrigerator could be made like a commercial product and try to apply thermoelectric materials to other applications. At is point, semiconductor thermocouples were also applied to real generators with a high output efficiency in some applications.

However, the performance of thermoelectric energy convertors has continued to remain inferior to that of the best standard machines [1].

Nowadays, ever-increasing attention is given to global energy issues and the rise wide-held consensus that a more sustainable society is needed to health and assure prosperity for future generations. These have moved the attention of engineers and scientists worldwide to more efficient, clean, and sustainable energy solutions. While applied thermoelectric generators are still far from being competitive compared with the standard electric generators [2-4] when used in combination with other generators, they allow for some of the waste heat to be recovered and then increase the general efficiency of the generators. Thermoelectric materials have therefore been recognized as a potential asset for converting direct its thermal energy to electrical energy in a variety of processes and vice versa.

The study of thermoelectric and its applications have also been widely considered as a solution to the low-high energy losses of the automotive and industrial sector. The transition to the new generation of electric or hybrid cars will take at least a couple of decades. Presently, the automobile industry must pay a lot of money to the EU for the emission of each additional gram of CO₂ above an established value that decreases every 3 to 4 years.

Thermoelectric materials on research and application are based on bismuth telluride (Bi₂Te₃) [5-8], lead telluride (PbTe) [9-11], silicon-germanium (SiGe) alloys [12, 13], iron di-silicide (FeSi₂) [14] and other compounds. At the present time, boron-based (B) and boron-carbon (B-C) materials have become promising thermoelectric materials for the development of a high-temperature range thermoelectric generator. Each thermoelectric material has its own temperature range of useful operating temperatures,

and its own definition depends on materials structure and properties.

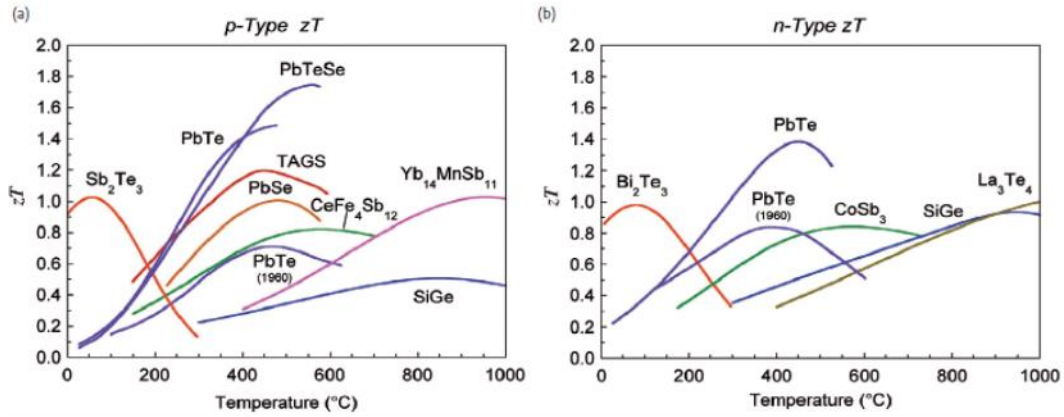


Figure 1.1 Overview of the figure of merit ZT of the most common thermoelectric materials versus temperature in degrees Celsius [15].

Figure. 1.1 shows the overview of ZT for thermoelectric materials in relation to the temperature in degrees Celsius [15]. **Figure. 1.1 (a)** includes the p -type and **Fig. 1.1 (b)** the n -type value for PbTe reported by Fritts in the 1960s. Lead chalcogenides (PbS , PbSe , PbTe) are useful for power generation in middle range temperature [16, 17]. In 1845, the first discovery of PbTe as a rare mineral altaite, while the more abundant galena (PbS) has been the main source of Pb ore since former times. In 1960, the peak of ZT about 0.8 for single-phase structure PbTe materials, have been successfully used for NASA spacecraft missions. They showed that the maximum ZT of ~ 1.4 is, in fact, intrinsic to both p -type and n -type materials. Increase in ZT has been achieved in alloys where ZT reaches a value approaching about 1.8 for PbSe and PbTe materials. Those reports are important to provide continuity to the further research and development of new ways to create the thermoelectric technology. PbTe material and compounds have been studied as high potential materials for the conduction of thermoelectric energy. Several comprehensive academic reviews of older research are reported in [18], while recent studies in PbTe nanostructure (including dopants) are mentioned in [19]. Researchers still try to improve the potential of PbTe materials, utilizing only small

concentrations of dopants (assuming the bands remain rigid), or alloys that produce only minor perturbations to tune the band structure.

In 1954, the first study of bismuth telluride (Bi_2Te_3) was reported by Julian Goldsmid [20]. A thermocouple was made from a *p*-type sample of the compound and then connected to a negative thermoelement. It was made from bismuth (Bi) and was found to yield a cooling effect of 26 K below ambient temperature as a consequence of the Peltier effect. In later years, *n*-type $\text{Bi}_2\text{Te}_{3-x}\text{Se}_x$ and *p*-type $\text{Bi}_{2-x}\text{Sb}_x\text{Te}_3$, which have an intrinsic *ZT* value of approximately 1.0 at 300 K, became one of the best thermoelectric materials for cooling applications and low-temperature power generation [21]. There were a few signs of progress made over the next several decades. That was widely accepted that its upper *ZT* limit was already reached. Anywise, in the last 15-20 years there have been notable advances due to an influx of many ideas for materials science, with new experimental techniques leading to higher *ZT* and low κ [22]. In 2008, Poudel et al. published a new technique for preparing $\text{Bi}_{0.5}\text{Sb}_{1.5}\text{Te}_3$ with a high relative density of grain boundaries, which involved hot pressing method of nano-powders [23]. *ZT* reached 1.4 at 373 K, it was prepared by nano bulk material with low κ ($\sim 1.0 \text{ W m}^{-1} \text{ K}^{-1}$) due to additional phonon scattering at the nanostructure grain boundaries. In 2015, Kim et al. reported a new preparation process for incorporating grain boundary dislocations into $\text{Bi}_{0.5}\text{Sb}_{1.5}\text{Te}_3$ thermoelectric materials, reaching *ZT* value of approximately 1.9 at 323 K [24]. However, this value has not been widely accepted. After this research, there are many ideas for a new research strategy. To understand more deeply the incorporating on of nano and meso-structure into bulk thermoelectric materials [25].

Recently, Hirota et al. [26] reported a carbon observation by electron energy-loss

spectroscopy of graphite added BiSbTe. Thermal conductivity of $(\text{Bi}_{0.3}\text{Sb}_{1.7}\text{Te}_{3.1})_{1-x}\text{C}_x$ increased slightly because the thermal conductivity of carbon is much higher than that of $\text{Bi}_{0.3}\text{Sb}_{1.7}\text{Te}_{3.1}$. In the study of *n*-type bismuth chalcogenides, progress has been slower. This is in large part since the electrical conductivity in these compounds are highly anisotropic. In 2014, Hu et al., reported a *ZT* value of approximately 1.2 at 445 K for $\text{Bi}_2\text{Te}_{2.3}\text{Se}_{0.7}$ produced by a new point-defect engineering materials strategy for reducing κ to lower than $1.2 \text{ W m}^{-1} \text{ K}^{-1}$ at 450 K [27]. Also, there are many *n*-type systems that have been reported to have high performance, such as confirmed by Han et al. [28]. As the research moves forward, it is very important to develop innovations for higher performance *n*-type thermoelectric materials to complement the advances made in *p*-type systems.

In fact, since the first time of the introduction of semiconductor thermoelements at the end of the twentieth century, there was little improvement in thermoelectric materials as mentioned. However, recently there are many ideas from scientists and engineers for the improvement of materials such as heavy doping, optimal dopant concentration, nanostructure and modern thermal diffusivity measurements for thermal conductivity that have been put forward, and significant advances are finally being made, at least on a university or research institute laboratory scale. It is reasonable to expect that thermoelectric materials will soon lead to a much wider application of the thermoelectric effects worldwide.

1.2 Performance evaluation of thermoelectric materials

Thermoelectricity is a niche research area in which various heat sources can be used to generate electricity. Thermoelectric materials are the cornerstone of commercial applications of electric generation, and there are many advances that have been made in fabricating materials with structures that improve thermoelectric performances [3, 29-33]. Almost all conducting materials have thermoelectric properties. Because the figure of merit varies with temperature, a more meaningful measure of performance is the dimensionless figure of merit ZT :

$$ZT = \alpha^2 \sigma \kappa^{-1} T \quad (1)$$

where α is the Seebeck coefficient (V K^{-1}),

σ is the electrical conductivity (S m^{-1}),

κ is the thermal conductivity ($\text{W m}^{-1} \text{K}^{-1}$),

and T is the absolute temperature (K).

Thermoelectric properties are the combination of electrical property, thermal property, and special coefficient of a material (Seebeck coefficient). The meanings and details of properties are follows:

-Seebeck coefficient, α

This property may be operationally defined as the electromotive force produced when a unit temperature difference exists between the points of measurement. Since the magnitude of the Seebeck coefficient directly determines the voltage developed by a thermoelectric generator (or, through the Peltier coefficient, the effectiveness of a heat-pumping device). The materials specifically developed for thermoelectric applications would have a Seebeck coefficient of approximately 100 to 400 $\mu\text{V K}^{-1}$.

- Electrical resistivity, ρ

Thermoelectric materials require low electrical resistivity because it increases the thermoelectric figure of merit. Normally, the semiconductors are used for thermoelectric material. Electrical conductivity (σ) is the reciprocal of the electrical resistivity (ρ).

- Thermal conductivity, κ

The thermoelectric applications require the lowest thermal conductivity attainable. The general semiconductors have thermal conductivity in the range 1 to 10 $\text{Wm}^{-1}\text{K}^{-1}$ and the range in metals is approximately an order of magnitude higher.

$$\kappa = \kappa_{\text{phonon}} + \kappa_{\text{carrier}} = \kappa_{\text{phonon}} + L\sigma T \quad (2)$$

Carrier thermal conductivity κ_{carrier} is given by the Wiedemann–Franz law, where κ_{phonon} and L are the phonon thermal conductivity and Lorenz number, respectively.

The Lorenz number of a metal is given by [34]:

$$L = (\pi k_B)^2 (3e^2)^{-1} = 2.45 \times 10^{-8} \text{ W S}^{-1}\text{K}^{-2} \quad (3)$$

Thermoelectric materials have been widely studied with many kinds of preparation methods that have been used to improve the ZT . The ZT values for well-known thermoelectric materials are among the highest values reported [35, 36]. Ideally, materials with thermoelectric properties should have high electrical conductivities and Seebeck coefficients, but low total thermal conductivity, i.e., a high power factor ($\alpha^2\sigma$) and low thermal conductivity are essential for maximizing the ZT value [37].

There are two primary strategies for improving ZT . One is optimization of the electronic term $\alpha^2\sigma\kappa_{\text{carrier}}^{-1}$, which is mainly governed by the local electronic structure (relaxation time, group velocity and density of states) near the Fermi level. The other way is reducing the phonon thermal conductivity κ_{phonon} by providing phonon-scattering centers, e.g., by introducing mass contrast and nanostructures in bulk materials [38, 39].

1.3 Lead telluride properties and literature review

PbTe thermoelectric materials perform well in the intermediate temperature range 450–850 K and have good chemical and thermal stabilities [40, 41]. PbTe crystallizes in the NaCl crystal (rock-salt) structure (halite, cF8), with Pb atoms occupying the cationic sites and Te forming an anionic lattice (space group Fm3m, No. 225), at constant room-temperature lattice constant of 6.462 Å (12.22 bohr), melting point at 1197 K and theoretical density of 8.26 g cm⁻³. It is a narrow band gap ($E_g \approx 0.25$ eV at 0 K, and 0.32 eV at 300 K) semiconductor, which can show either *p*-type or *n*-type semiconductor conductivity depending on the deviation from stoichiometry. PbTe has a large exciton Bohr radius of approximately 46 nm, which leads to charge carrier confinement in relatively large nanostructures [42]. The reported values for the carrier concentration and Seebeck coefficient of high-purity undoped PbTe are similar to the published theoretical values [10].

PbTe based alloys are promising thermoelectric materials because of high dependence on carrier concentration, low κ and high-power factors. However, because of fracture susceptibility, PbTe materials are difficult to process and have limited applications [43, 44]. To overcome the mechanical and thermal stresses, the reduction of PbTe grain size is an effective hardening mechanism [45].

Ball milling process is required for achieving small grain sizes and particles. This preparation process can introduce defects into the crystal lattice that act as dopants and change the electronic properties. After sintering process, materials structure can produce grain growth and partial repair of defects caused by milling [46]. An earlier study reported on undoped PbTe prepared by mechanical alloying (MA) with a Si₃N₄ vessel and balls milled at 596 rpm produced powder with minimum size at 3 h milling [47].

That research compared powder microstructure and sintered morphology for sintering temperatures of 923 K (76% relative densities) and 1023 K (79% relative densities). Differential scanning calorimetry (DSC) showed MA to be associated with exothermic reaction heat between Pb and Te that promotes the rapid formation of PbTe and allows a 3 h milling time for obtaining PbTe stoichiometric samples [48]. At 6-31 h milling times, crystallite size decreases and saturates to a value around 260 Å. After 31 h milling time, crystallite size slightly increased again. There are reports showing that microstrain should increase with milling time [49]. However, research on powder does not sufficiently clarify the electrical properties, grain sizes, and microstrain of bulk materials after sintering.

Theoretical calculations based on a grain boundary scattering show that the κ_{phonon} of undoped bulk PbTe at 400 K is constant from coarse grains to average size 1 μm and then sharply decreases at grain size of 0.01 μm [50, 51]. These figures of merit should improve in materials with reduced grain size. Theoretical analysis shows that the κ of undoped PbTe with grain size of 1 μm is approximately 5% lower than in similar material with larger grain size [52]. Low κ_{phonon} in PbTe may be due to many factors. A recent report established the importance of lattice softening in thermal transport and internal strain induced by ball milling [53]. Increase in internal strain corresponds with linear decrease in the speed of sound. Softening of the material lattice is the only scattering mechanism that reduces κ_{phonon} .

Repeated mechanical impact during planetary ball milling followed by hot pressing (MG-HP) is a powerful method for preparing homogeneous compounds that enables the formation of alloys in solid-state. For polycrystalline PbTe materials, synthesis is performed in an evacuated and sealed quartz tube. This conventional synthesis is

restrictive for industrial applications because the process is long and requires high temperatures. Powder metallurgy based on MG-HP is frequently used in preparation. The effect of rotation speed of ball mill on thermoelectric properties in undoped PbTe with fine grain, low κ_{phonon} , high purity, and relative density (more than 99%) has not received sufficient study.

Mechanical alloy processing and hot pressing (MA-HP) produces thermoelectric materials without melting [54]. High energy milling activates local reaction among elements when raw materials are sufficiently refined and close in proximity. MA produces high exothermic heat as Pb and Te react and grain boundary scattering produces a refining effect. To maintain low κ_{phonon} , fine grained material is normally prepared using MA or another powder metallurgy. MA followed by HP can synthesize materials with uniform element distribution.

Ball milling produces powder with small grain size, which decreases κ and improves ZT [55-58]. Improvement in thermoelectric performance can be used to determine grain boundary scattering in bulk materials [59, 60] because milling rotation speed improves thermoelectric properties. PbTe thermoelectric materials made of powder by processes such as MG and MA have uniform element distribution compared to conventional melt crystal growth alloys [61]. However, the most efficient preparation process is still unknown.

The present study focused on samples of undoped bulk PbTe, which were prepared by a powder metallurgy method. The effects of the planetary ball milling through various rotational speed on the thermoelectric properties of samples prepared by MG and MA followed by HP were investigated. The use of a planetary ball mill to achieve fine grain sizes can reduce the κ_{phonon} . Grain refinement by MG-HP and MA-HP improves the

performance of a thermoelectric material by decreasing the κ_{phonon} .

1.4 Bismuth antimony telluride properties and literature review

At room temperature, high ZT values in Bi_2Te_3 -based materials is ~ 1.0 . This material is used in wearable thermoelectric devices and harvesting power generation [62]. Bi_2Te_3 -based materials have a rhombohedral crystal structure and belong to the anisotropic physical, $R3m$ space group properties. Much research has focused on developing preparation methods that improve higher ZT for Bi_2Te_3 -based materials [63]. There are two main strategies. One involves high-pressure torsion and hot extrusion [64] since anisotropic thermoelectric properties can be obtained by plastic deformation under anisotropic preparation states. Another involves dopant addition of other elements [65], nanostructures dispersion [66], and ball milling such as mechanical grinding or alloying [5, 26] by powder metallurgy [7] under isotropic preparation states. After ball milling, the microstructure and electrical properties of materials depend on the milling energy during the ball milling process, particles size, composition, the size distribution of the ball milling materials [67]. A large powder grains size can be produced by high milling energy and at high temperatures. There is a lack of relationships among the milling energy in different rotation speed, different sintering conditions by hot pressing have not been reported. The difference in milling energy depends on the ball milling materials and rotation speed.

In a recent study [68], p -type $\text{Bi}_{0.3}\text{Sb}_{1.7}\text{Te}_{3.0}$ prepared by milling process with stainless-steel vessel and Si_3N_4 balls at various rotation speeds followed by hot pressing, reached a ZT value of approximately 1.01 at room temperature. However, with this milling condition, there is contamination of iron and chromium. Thermoelectric properties were harmfully affected by the milling process [68]. In reference to these

problems, we made changes to the milling vessels and balls, to prevent the contamination during the milling process. Yttria-stabilized zirconia (YSZ) ceramics vessel and ball are suitable materials for milling conditions, with high fracture toughness that led to higher ZT and low contaminations. [69].

1.5 Research objectives

1. Synthesis and characterization of thermoelectric properties of lead telluride, prepared by ball milling (BM) at various rotation speed (stainless-steel vessel (Fe–Ni–Cr) and Si₃N₄ balls) and followed by hot pressing.
2. Study on the grain size and phonon thermal conductivity in undoped lead telluride processed by mechanical grinding (MG) and alloying (MA) using yttria-stabilized zirconia (YSZ) ceramic vessels and balls.
3. Synthesis and characterization of thermoelectric properties of *p*-type Bi_{0.3}Sb_{1.7}Te_{3.0}, prepared by a mechanical alloying (MA) followed hot pressing with a YSZ ceramics vessel and balls. Relationships among the sintering conditions and milling energy were investigated.

CHAPTER 2

EXPERIMENTATION AND METHODOLOGY

2.1 PbTe materials and preparation methods.

2.1.1 “Synthesis and characterization of thermoelectric properties of lead telluride, prepared by ball milling (BM) at various rotation speed (stainless-steel vessel (Fe–Ni–Cr) and Si₃N₄ balls) and followed by hot pressing”.

Melting–HP and ball milling (BM)–HP samples of PbTe were prepared by melting and dry ball milling followed by HP, respectively. Raw materials, i.e., Pb (99.998%, 3–5 mm grain size) and Te (99.9999%, 2 mm grain size) were purchased from the Kojundo Chemical Laboratory Co., Ltd. PbTe ingots were produced by melting in evacuated quartz ampoules. The inner diameter and length of the carbon-coated ampoule were 10 mm and 120 mm, respectively, and the bottom end was columnar-cone-shaped. The raw materials were placed in the ampoule, which was sealed under 0.1 Pa. The ampoule was heated to 1123 K by an electric furnace. The temperature was maintained for 3 h and then the reaction was quenched with water.

The PbTe ingots were placed in a stainless-steel vessel (Fe–Ni–Cr) with Si₃N₄ ceramics balls (25 mm diameter). Weight ratio of milling balls to ingots was more than 20:1. BM with the Si₃N₄ ceramics balls was performed by Fritsch P-5 planetary ball mill, and milled at maximum rotation speed of 180 rpm for 30 h. Stainless-steel vessel was sealed in a glove box under Ar atmosphere to prevent powder oxidation during the milling process. For each sample, milling was performed at 90–180 rpm for 30 h.

After milling, milled powder was passed through a 150 μm diameter sieve to separate the unmilled material. The PbTe ingot (prepared at 0 rpm) and the milled powder were then compacted by HP at 650 K under a uniaxial pressure of 147 MPa. Powders were

prepared in an Ar atmosphere, except when the HP mold was exposed to air during transfer between the Ar-filled glove box to HP chamber. Hot-pressed and sintered compacts, which were 8–10 mm thick and 10 mm in diameter, were cut into disks of thickness ~ 1 mm, and diameter 10 mm, and used for determining the Seebeck coefficients, electrical and thermal conductivities of the samples. The cut PbTe disk densities were determined by Archimedes' method, with a relative density accuracy better than $\pm 0.2\%$.

2.1.2 “Study on the grain size and phonon thermal conductivity in undoped lead telluride processed by mechanical grinding (MG) and alloying (MA) using yttria-stabilized zirconia (YSZ) ceramic vessels and balls”.

Mechanical grinding (MG)–HP samples of PbTe were prepared by melting and dry ball milling and followed by HP. Ingots produced by MG were synthesized from high-purity Pb (99.998%, grain size 3–5 mm) and high-purity Te (99.9999%, grain size 2 mm) from the Kojundo Chemical Laboratory Co., Ltd. Stoichiometric amounts of these elements for targeted PbTe compositions were placed in clean carbon-coated ampoules with columnar-cone-shaped bottom (10 mm inner diameter, 120 mm length). Raw materials for MG samples were placed in ampoules and the ampoules were sealed under 0.1 Pa. MG ingots obtained were heated to 1123 K by an electric furnace. The temperature was maintained for 5 h and quenching was in water at room temperature.

The melting process was not applied to MA-HP samples. MG ingots and raw materials for MA were placed in yttria-stabilized zirconia (YSZ) ceramic vessels (0.25 L capacity) and balls (25 mm diameter). Weight ratio of milling balls to ingots and raw materials was 20:1. Milling was performed with a Fritsch P-5 planetary ball mill. Vessels and ball were sealed in a glove box under Ar atmosphere to prevent powder oxidation during the milling process. Milling was performed at 90–180 rpm for 30 h in an Ar filled glove box and milled powder was passed through a polymer mesh sieve (150 μ m diameter) to separate milled and unmilled materials. After separation, powder was put in an HP mold. HP chamber was evacuated below 0.4 Pa and then compacted in Ar atmosphere at 650 K under uniaxial pressure of 147 MPa.

BiSbTe materials and preparation methods

2.2 “Synthesis and characterization of thermoelectric properties of *p*-type Bi_{0.3}Sb_{1.7}Te_{3.0}, prepared by a mechanical alloying (MA) followed by hot pressing with a YSZ ceramics vessel and balls”.

Composition of the milled powder was stoichiometric, i.e., Bi_{0.3}Sb_{1.7}Te_{3.0} [43]. High-purity elements of Bi (99.999%), Sb (99.9999%), and Te (99.9999%) of several grain sizes (all purchased from the Kojundo Chemical Laboratory Co., Ltd). Raw materials were weighed following the formula Bi_{0.3}Sb_{1.7}Te_{3.0} and were set in YSZ vessel with milling balls in an argon-filled glove box. YSZ vessels (0.25 L capacity, 25 mm diameter) were sealed inside the box to keep vessels safe from the air. The main reason to use YSZ vessel and milling balls was because we need to avoid reactions with the milled powder during the milling process. Various milling rotation speeds gave partial to complete alloy materials. Thermoelectric properties of Bi_{0.3}Sb_{1.7}Te_{3.0} at various mill rotation speeds on the degree of alloying were investigated. Handling procedures and weight ratio of milling balls to raw materials were the same as those previously studied using a stainless-steel vessel and Si₃N₄ balls [68].

Milling process was performed at 110-180 rpm for 30 hours. Ratio of the rotation speed of the planetary disk to that of the milling vessel was fixed at 1: -2.18. After milling process, milled powder was passed through a polymer mesh sieve (150 μm diameter) to separate milled and unmilled materials. This process was to assure that no elemental grains remained on the polymer mesh sieve in each preparation. Milled powder was investigated by x-ray diffraction machine (XRD; Rigaku Smart Lab, Cu K α radiation) to confirm alloying after milling process. This process considered whether contamination caused by erosion of the vessel and milling balls occurred. Bi_{0.3}Sb_{1.7}Te_{3.0} milled powder

at minimum rotation speed was used to consider the effects of milling vessel and ball, and HP sintering temperature.

After separation by polymer mesh sieve, the powder was put in an HP mold. HP chamber was evacuated below 0.4 Pa and then compacted in Ar atmosphere at target sintering temperature under uniaxial pressure of 147 MPa. Samples were prepared in Ar atmosphere, except when HP mold was exposed to air during transfer between the glove box to HP chamber. Relationships between metallography, microstructure, electrical properties, and sintering temperature in bulk materials were investigated.

The significant of sintering temperature for the minimum rotation speed needed to achieve complete alloying of the milled materials. A study on sintering temperature can find a good condition for thermoelectric properties and improve achievement. $\text{Bi}_{0.3}\text{Sb}_{1.7}\text{Te}_{3.0}$ milled at the minimum rotation speed was sintered at 100 - 400 °C under uniaxial pressure of 147 MPa. Sintered ingots (8–10 mm thickness, 10 mm diameter) were cut into disks (~1 mm thickness, 10 mm diameter). Disks obtained from the ingot ends were not used for measurements because there was affected by plastic deformation, and have anisotropic properties as a result of HP [70].

2.3 X-ray diffraction

PbTe and BiSbTe samples structures were investigated by X-ray diffraction machine (XRD; Rigaku SmartLab, Cu K α radiation), and scanning electron microscopy (SEM; JEOL, JSM-6510A), and focused ion beam (FIB; JEOL, JEM-9320) system. XRD patterns for those of PbTe sintered samples were recorded in the Bragg angle range $2\theta = 20^\circ\text{--}90^\circ$ and $20^\circ\text{--}110^\circ$ for BiSbTe samples. General scans with a step size of 0.1° and a step time of 0.5 s were conducted for phase identification. Crystallite size was based on the Scherrer equation. Microstrain was determined using the most intense reflection for the full width at half maximum (FWHM) for microstrain analysis in PbTe.

2.4 Microstructures, grain sizes and EDS

The microstructures and grain sizes of PbTe cross-sections were examined by FIB-SEM, SEM, and energy-dispersive x-ray spectroscopy (EDS). The surfaces of the PbTe sintered disks were polished and slightly chemically etched. An agglomerate-free alumina powder and alumina suspension were used as polishing grits. Average grain sizes were observed by FIB-SEM and measured by the linear intercept technique for two-phase polycrystals [71]. The elemental dispersion profiles of PbTe cross-sections were determined by EDS.

The microstructures for Bi_{0.3}Sb_{1.7}Te_{3.0} sintered disks at 100 and 350 °C were examined by scanning electron microscopy (SEM; JEOL, JSM-6510A). At the same area, elemental distribution profiles of cross-sections were examined by energy-dispersive x-ray spectroscopy (EDS).

2.5 Electrical conductivity

Electrical conductivity was measured by a four-point probe method with a delta-mode electrical resistance system based on a 2182A/6220 instrument (Keithley Instruments, Inc.) Probe was made of tungsten carbide of size 1.0 mm. All measurements made using the electrical conductivity system were confirmed by ohmic contact to be of accuracy better than $\pm 1\%$.

2.6 Seebeck coefficient

Seebeck coefficient was determined using a constructed [72] thermal contact system. Use of a standard BiTe thermoelectric material (SRM 3451) as a reference sample confirmed that accuracy was better than $\pm 2\%$ at room temperature.

2.7 Thermal conductivity

Thermal conductivity was measured using a constructed [73] static comparison method system. Quartz ($\kappa = 1.411 \text{ W m}^{-1} \text{ K}^{-1}$) was used as a reference sample, and the accuracy was better than $\pm 1\%$. Measured sample and quartz were sandwiched between copper blocks of 10 mm in diameter for thermal conductivity static comparison.

2.8 Dimensionless figure of merit ZT

ZT was calculated from the room temperature of Seebeck coefficient, electrical and thermal conductivity follow equation (1).

CHAPTER 3

RESULTS AND DISCUSSION

3.1 PbTe results and discussion

3.1.1 “Synthesis and characterization of thermoelectric properties of lead telluride, prepared by ball milling (BM) at various rotation speed (stainless-steel vessel (Fe–Ni–Cr) and Si₃N₄ balls) and followed by hot pressing”.

Hot-pressed samples were *p*-type semiconductors according to measurement of Seebeck coefficient. **Table 3.1.1** shows absolute and relative densities of Melting–HP and BM-HP samples measured by Archimedes’ method [41]. Samples had relative density of close to 99%. Density did not depend on rotation speed. Thermoelectric properties of sintered materials depended on density or porosity. High porosity changes electrical and thermal conductivity. Samples in this research were compact enough to resist changes.

Table 3.1.1 Milling rotation speed and density of Melting–HP and BM–HP samples.

Milling rotation speed (rpm)	Absolute density $\rho / 10^{-3} \text{ kg m}^{-3}$	Relative density (%)
Melting-HP	8.24	99.8
90	8.21	99.4
110	8.21	99.4
120	8.22	99.5
150	8.23	99.6
180	8.20	99.3

Theoretical density $8.26 \times 10^{-3} \text{ kg m}^{-3}$ [41].

Figure 3.1.1 shows XRD patterns in the 2θ range of 20° – 90° for Melting-HP and BM-HP samples. PbTe main indexes were added to the patterns [41]. XRD pattern peaks indicated single-phase PbTe crystal structures and there were no peaks from other materials.

Figure 3.1.2 shows full width at half maximum (FWHM) fixed on (200) peaks as a function of milling rotation speed for BM-HP samples. Sample milled at 120 rpm had most internal strain. FWHM is generally proportional to the internal strain. In this study, samples milled at 120 rpm had the highest internal strain.

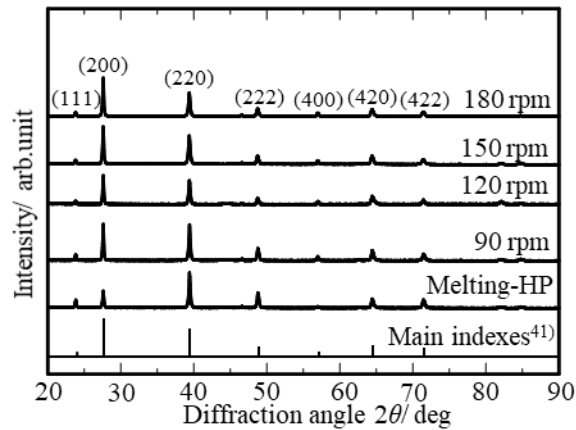


Fig. 3.1.1 XRD patterns of PbTe Melting-HP and BM-HP samples milled at rotation speed from 90 to 180 rpm and PbTe main indexes⁴¹⁾.

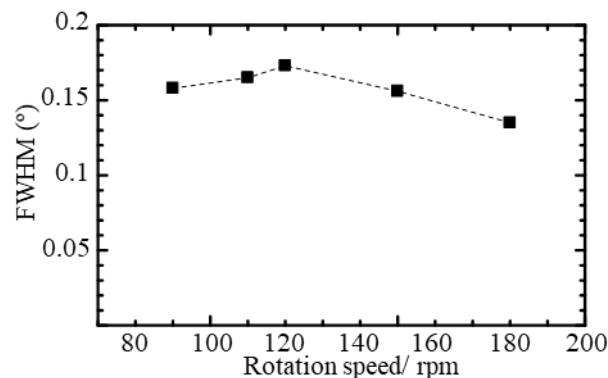


Fig. 3.1.2 Full width at half maximum (FWHM) at (200) peaks as a function of milling rotation speed for PbTe samples prepared by BM-HP.

Figure 3.1.3 shows FIB-SEM micrographs of Melting-HP and BM-HP samples milled

at 90, 120, 150 and 180 rpm. Samples had dense and fine grain structures. Measured by the linear intercept technique [71], the Melting-HP sample had 22.62 μm average grain size. For BM-HP samples, average grain size decreased with increasing rotation speed: 1.15 μm at 90 rpm, 0.80 μm at 120 rpm, 0.72 μm at 150 rpm and 0.66 μm at 180 rpm.

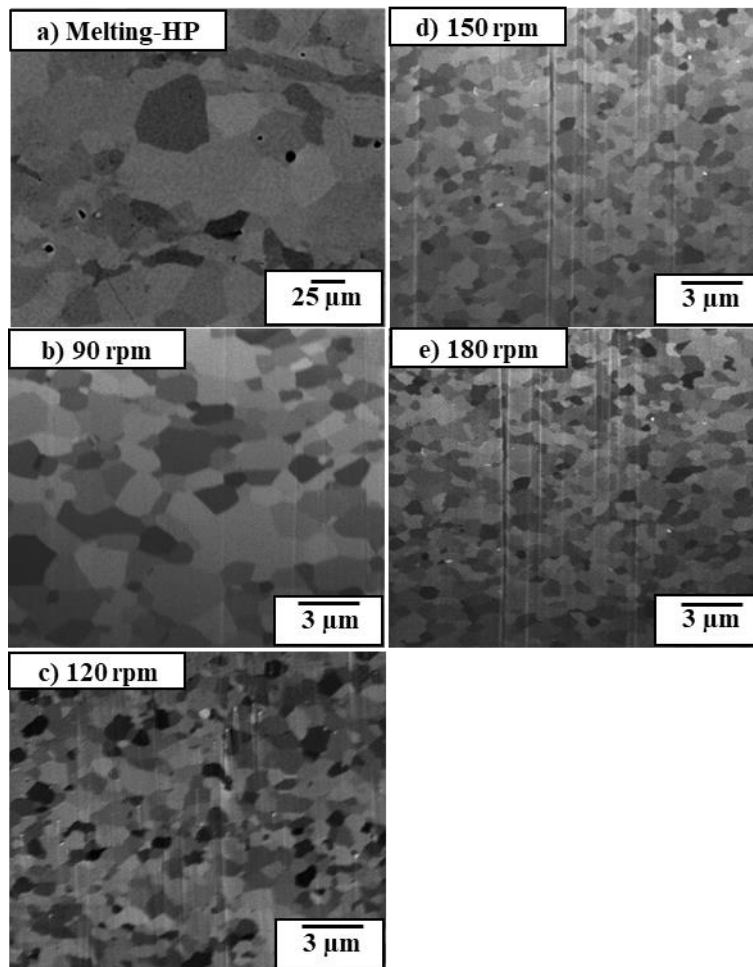


Fig. 3.1.3 FIB-SEM micrographs of (a) Melting-HP and BM-HP samples milled at (b) 90 rpm, (c) 120 rpm, (d) 150 rpm and (e) 180 rpm.

Figure. 3.1.4 shows electrical conductivity σ at room temperature of Melting-HP and BM-HP samples as a function of milling rotation speed. Electrical conductivity in Melting-HP was similar to the electrical conductivity in the BM-HP sample milled at 90 rpm. Electrical conductivity of BM-HP samples increased with rotation speed. Iron (Fe), chromium (Cr), and nickel (Ni) contaminants are estimated to act as *p*-type dopants.

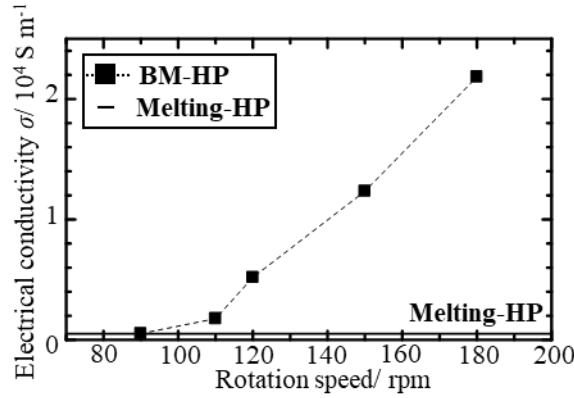


Fig. 3.1.4 Electrical conductivity σ at room temperature of Melting-HP and BM-HP as a function of milling rotation speed for PbTe samples.

Figure. 3.1.5 shows concentration of Fe, Cr, and Ni elements in PbTe samples determined by ICP-OES. The concentration of impurities increased with rotation speed. Results in **Figure. 3.1.4** and **Figure. 3.1.5** are consistent relationship between carrier concentration and electrical conductivity. Increase in electrical conductivity was likely because of contamination from the milling vessel.

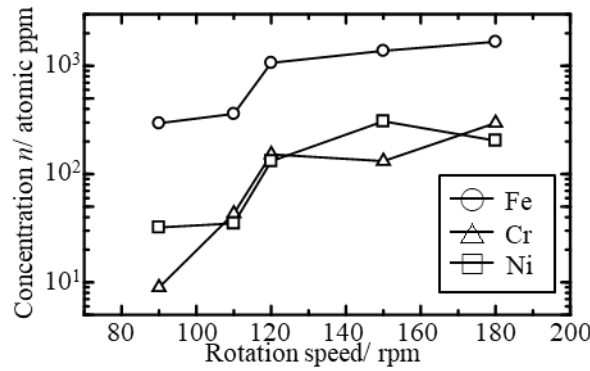


Fig. 3.1.5 Concentration of Fe, Cr and Ni elements as a function of milling rotation speed for PbTe samples prepared by BM-HP.

Figure. 3.1.6 shows total thermal conductivity (κ_{total}), phonon component (κ_{phonon}) and carrier component (κ_{carrier}) at room temperature of Melting-HP and BM-HP samples as a function of milling rotation speed. κ_{phonon} and κ_{carrier} values were estimated from eqs. (2) and (3) (see Introduction). κ_{phonon} values for PbTe samples prepared by Melting-HP and BM-HP at a rotation speed of 90 rpm were almost the same in terms of electrical

conductivity. At 120 rpm, BM-HP sample had minimum κ_{phonon} value of $1.29 \text{ W m}^{-1} \text{ K}^{-1}$ and average grain size of $0.80 \mu\text{m}$. The κ_{phonon} in PbTe decreased from 90 rpm to 120 rpm, increased from 120 rpm to 150 rpm and remained relatively constant from 150 rpm to 180 rpm. There was a significant inverse relationship between κ_{phonon} and FWHM (see **Figure 3.1.2**).

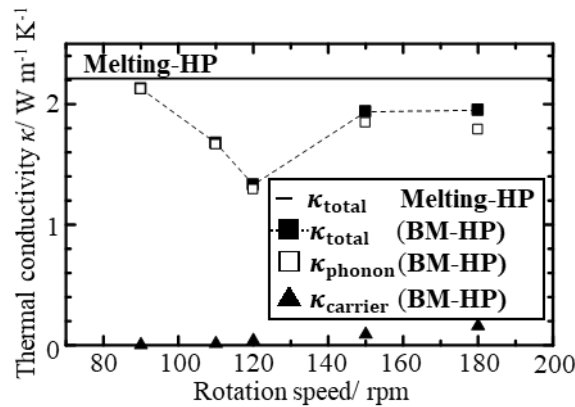


Fig. 3.1.6 Total thermal conductivity (κ_{total}), phonon (κ_{phonon}) and carrier (κ_{carrier}) components at room temperature of Melting-HP and BM-HP as a function of milling rotation speed for PbTe samples.

Figure 3.1.7 shows the relationship between average grain size and phonon thermal conductivity κ_{phonon} at room temperature of Melting-HP and BM-HP for PbTe samples. The calculated κ_{phonon} by grain boundary scattering was constant from coarse grain size to average grain size of $1 \mu\text{m}$. The critical point in κ_{phonon} change occurred when grain size was approximately $0.03 \mu\text{m}$ at 400 K [50, 51]. The present study showed that at rotation speed of up to 120 rpm, κ_{phonon} value in PbTe samples decreased as rotation speed increased because grain size was less than $1 \mu\text{m}$. Such decreasing behavior agreed with theoretical calculation [50, 51]. However, the observed critical point around $1 \mu\text{m}$ differed from theoretical calculation by grain boundary scattering. High rotation speed produced internal strain in small grain size. The internal strain such as dislocations and

lattice defects changed phonon frequencies within the material [53]. Internal strain was confirmed in PbTe samples prepared by BM-HP, with internal strain peaking at 120 rpm (see Fig. 3.1.2).

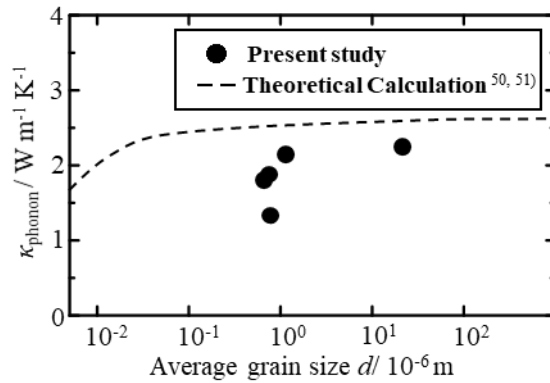


Fig. 3.1.7 Relationship between average grain size and phonon thermal conductivity κ_{phonon} at room temperature of Melting-HP and BM-HP for PbTe samples. The solid line is the calculated phonon thermal conductivity by grain boundary scattering at 400 K^(50, 51).

From these results, κ_{phonon} of PbTe was constant from coarse grain size to average size of 1 μm and decreased in grain sizes below 1 μm . Minimum κ_{phonon} was at 120 rpm in PbTe, which led to peak internal strain. Rotation speed affected thermoelectric properties.

3.1.2 “Study on the grain size and phonon thermal conductivity in undoped lead telluride processed by mechanical grinding (MG) and alloying (MA) using yttria-stabilized zirconia (YSZ) ceramic vessels and balls”.

Preliminary XRD showed that processed milled powder had single-phase alloy. After hot-pressing, all PbTe samples prepared by MG-HP and MA-HP were dense and *p*-type semiconductors. **Table 3.2.1** shows milling rotation speed depends on the absolute and relative densities of MG-HP and MA-HP samples measured by Archimedes’ method [41]. Samples prepared by the MG-HP process had relative density close to 99%, higher than results in another report [47]. MA-HP samples were above PbTe theoretical bulk density because the interior temperature of the milling vessel rose due to high exothermic reaction heat between Pb and Te [48]. Te had higher vapor pressure than PbTe and Pb, and Te evaporated during the milling process [41]. Vapor pressure of PbTe, Pb and Te were less than 10^{-6} , 10^{-5} , and 1 Pa at 650 K [74, 75], respectively.

Table 3.2.1 Milling rotation speed and densities of MG-HP and MA-HP PbTe samples.

Rotation speed (rpm)	Absolute density $\rho/ 10^{-3} \text{ kg m}^{-3}$, relative density (%)	
	MG-HP	MA-HP
90	8.23, 99.7	8.33, 100.9
110	8.23, 99.7	8.30, 100.5
120	8.20, 99.3	8.30, 100.5
140	8.21, 99.4	8.36, 101.3
150	8.21, 99.4	8.40, 101.7
160	8.22, 99.6	8.38, 101.5
180	8.24, 99.9	8.39, 101.5

Theoretical density $8.26 \times 10^{-3} \text{ kg m}^{-3}$ [41].

Figure. 3.2.1 (a) show SEM image of the PbTe sample sintered at 650 K and milled at 150 rpm followed by MG-HP. Except for the dark particles, the matrix was dense and there was uniform elemental distribution without pores or voids. **Figure. 3.2.1 (b)–(f)** shows elemental distributions of Pb, Te, Zr, Y, and O determined by EDS. A dark particle with diameter of around 2 μm in **Figure. 3.2.1 (a)** shows erosion from the YSZ vessel and balls. Also, in MA-HP sample milled at 150 rpm was observed a uniform elemental distribution and particles caused by erosion from the YSZ vessel and balls.

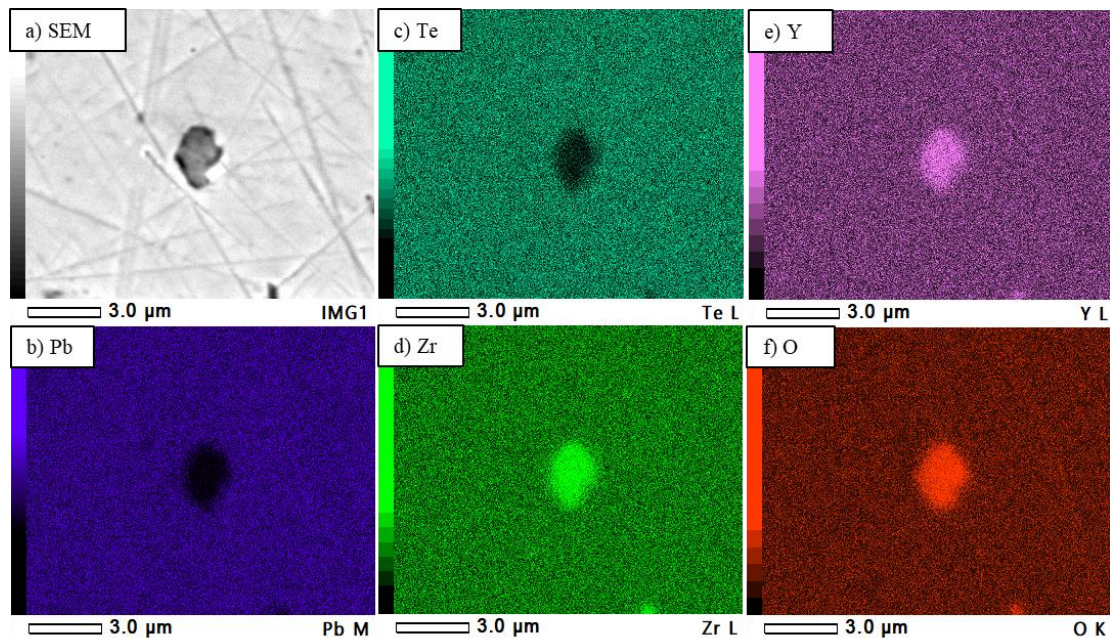


Fig. 3.2.1 EDS-derived elemental distribution of a PbTe sample milled at 150 rpm prepared by MG-HP. (a) SEM image, (b) Pb, (c) Te, (d) Zr, (e) Y and (f) O.

Figure. 3.2.2 (a)-(c) shows FIB-SEM micrographs of MG-HP and **Figure. 3.2.2 (d)-(f)** for MA-HP, PbTe milled at 90, 150 and 180 rpm sintered at 650 K. PbTe samples had dense and fine grains. Linear intercept technique [71] was applied to calculate the average grain size of PbTe samples prepared by MG-HP and MA-HP (**Figure. 3.2.3**). Average grain size decreased, and grain saturation increased with rotation speed. Minimum average grain size was obtained with 0.47 μm milling at 150 rpm for PbTe

sample produced by MG-HP. Minimum average grain size was obtained with 0.52 μm milling at 120 rpm produced by MA-HP. Average grain size at 140-180 rpm for MA-HP were slightly higher than for MG-HP due to exothermic reactions heat in the MA process [48]. The MG process produced kinetic energy while the MA process produced kinetic energy together with high exothermic reaction heat [48].

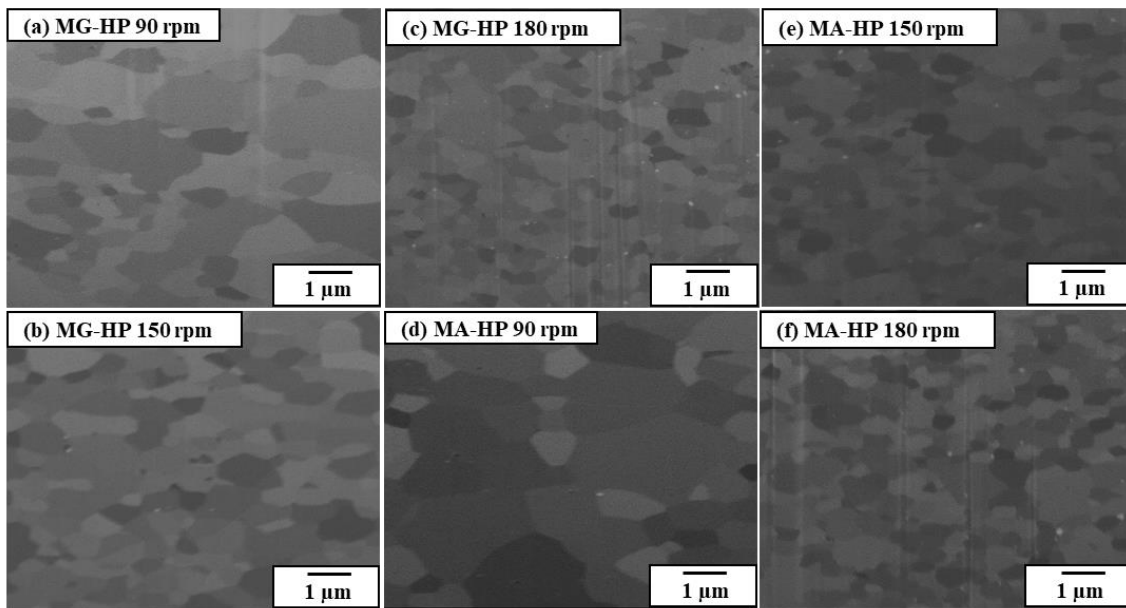


Fig. 3.2.2 FIB-SEM micrographs of PbTe samples prepared by MG-HP from (a)-(c) and MA-HP from (d)-(f) at 90, 150 and 180 rpm.

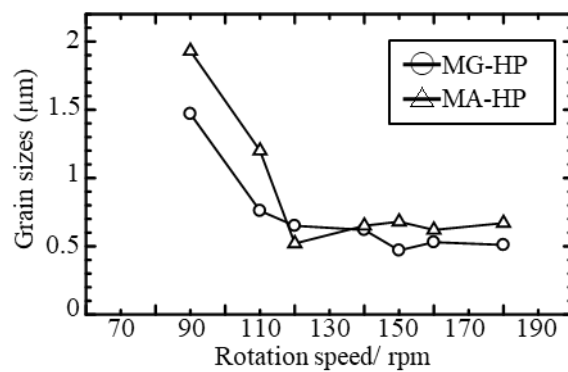


Fig. 3.2.3 Grain sizes (μm) and milling rotation speed related to PbTe samples prepared by MG-HP and MA-HP.

Figure 3.2.4 and **Figure 3.2.5** show a sequence of XRD patterns in the 2θ range 20° – 90° for PbTe MG–HP and MA–HP samples milled at rotation speed of 90 to 180 rpm and PbTe main indexes [41]. XRD pattern peaks show that PbTe samples had single-phase crystal structures, no peaks from other materials were observed. XRD patterns were determined using the main reflection (200) for full width at half maximum (FWHM) and crystallite size (\AA).

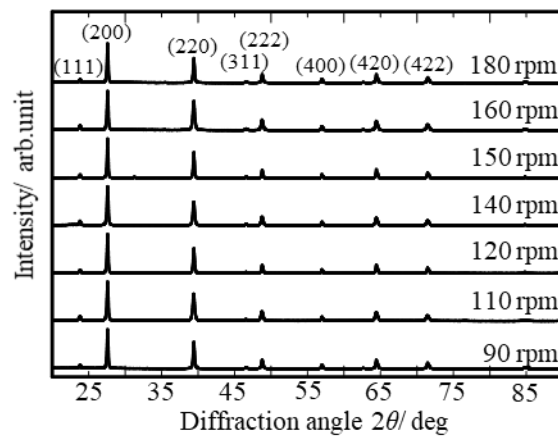


Fig. 3.2.4 XRD patterns of PbTe MG–HP samples milled at rotation speed from 90 to 180 rpm, and PbTe main indexes [41].

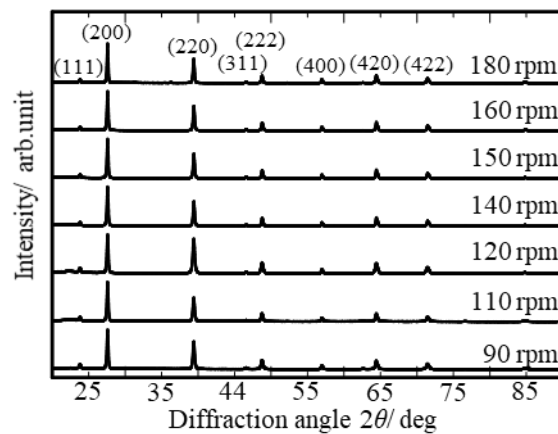


Fig. 3.2.5 XRD patterns of PbTe MA–HP samples milled at rotation speed from 90 to 180 rpm, and PbTe main indexes [41].

Figure. 3.2.6 and **Figure. 3.2.7** in MG-HP, the microstrain considered by FWHM tended to increase with milling rotation speed while crystallite size decreased and became finer. At 90-120 rpm, the microstrain for MA-HP was slightly higher than for MG-HP. At 140-180 rpm, the high exothermic reaction heat relaxed the microstrain in MA-HP samples and increased crystallite size. The observations agreed with our results as [49], by Neutron powder diffraction analysis for PbTe powder depended on milling times was indicated increased in crystallite size.

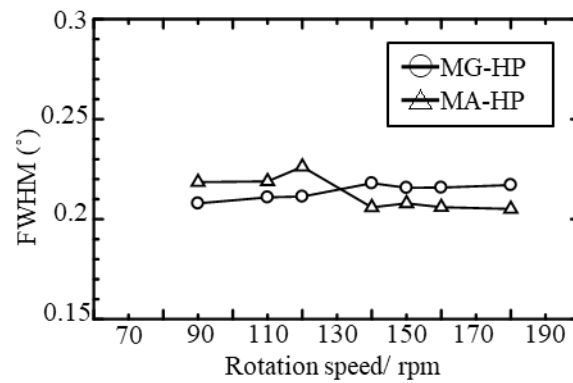


Fig. 3.2.6 Full width at half maximum (FWHM) at (200) index and milling rotation speed related to PbTe samples prepared by MG-HP and MA-HP.

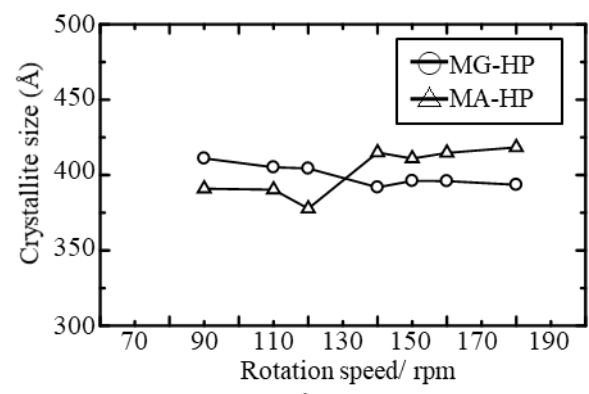


Fig. 3.2.7 Crystallite size (Å) and milling rotation speed related to PbTe samples prepared by MG-HP and MA-HP.

Figure. 3.2.8 shows electrical conductivity σ at room temperature and milling rotation speed related to PbTe samples prepared by MG-HP and MA-HP. The open circles and open triangles show the electrical conductivity produced by MG-HP and MA-HP, respectively. Electrical conductivity of MG-HP and MA-HP increased with the milling rotation speed. Because the milling kinetic energy converted to thermal energy, thermal energy caused Te evaporation. Te vapor pressure is higher than vapor pressure of Pb and PbTe [74, 76]. Evacuation of Te probably leads to Te deficiency in PbTe during high rotation speed. Electrical conductivity of PbTe samples produced by MA-HP was higher than the MG-HP. During the milling process, MA-HP produced more milling energy and more exothermic reaction heat than MG-HP. The reaction between Pb and Te heated the milling vessel interior due to high exothermic heat [48]. The large quantity of Te deficiency created during the milling led to an increase in electrical conductivity. However, Te deficiency might be at the limit of solid solution for PbTe as shown in **Figure. 3.2.4** and **Figure. 3.2.5**. The effect of Te deficiency was consistent with MA-HP samples having a relative density above the theoretical density in **Table. 3.2.1**.

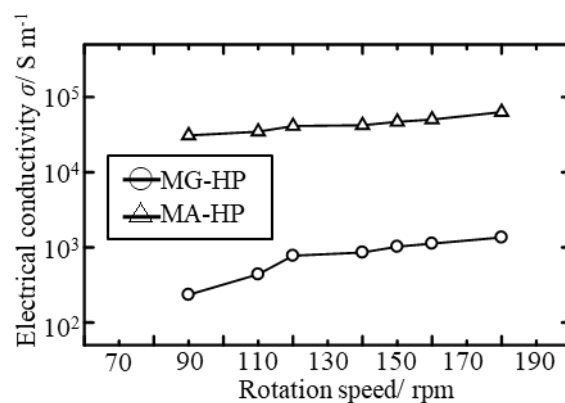


Fig. 3.2.8 Electrical conductivity σ at room temperature and milling rotation speed related to PbTe samples prepared by MG-HP and MA-HP.

Figure. 3.2.9 shows Seebeck coefficient α at room temperature and milling rotation

speed related to PbTe samples prepared by MG-HP and MA-HP. The open circles and open triangles show the Seebeck coefficient produced by MG-HP and MA-HP, respectively. For MG-HP samples, Seebeck coefficient decreased as rotation speed increased. The maximum value $494 \mu\text{V K}^{-1}$ of Seebeck coefficient was obtained with MG-HP sample milled at 90 rpm. Seebeck coefficient of MA-HP samples slightly decreased at high rotation speed and was lower than the Seebeck coefficient of samples prepared by MG-HP. Te deficiency acts as dopant and reduces the Seebeck coefficient. MG-HP process prevents Te evaporation, so MG-HP samples have a high Seebeck coefficient near stoichiometry of PbTe. Seebeck coefficient of MG-HP samples decreased with increased rotation milling speed, especially at 150-180 rpm. Increased milling energy could be because as in **Figure. 3.2.8**, Te evacuation during the milling led to Te deficiency in PbTe at 150-180 rpm. For MG-HP samples, Seebeck coefficient decreased because Te deficiency created during the high energy milling vessel, which is consistent with the dependences of electrical conductivity and Seebeck coefficient on the concentration of free carriers [30]. Because Te deficiency acts as dopant, electrical conductivity and Seebeck coefficient in MA-HP samples behaved like *p*-type doped materials.

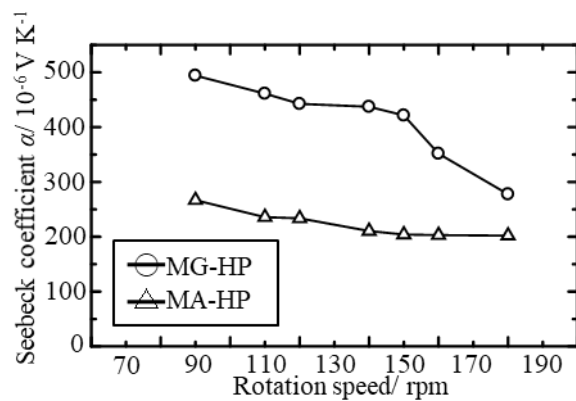


Fig. 3.2.9 Seebeck coefficient α at room temperature and milling rotation speed related to PbTe samples prepared by MG-HP and MA-HP.

Figure. 3.2.10 shows the total thermal conductivity κ_{total} and phonon thermal conductivity κ_{phonon} at room temperature and milling rotation speed related to PbTe samples prepared by MG-HP and MA-HP. The κ_{phonon} values were estimated from equations (2) and (3) and showed that κ_{phonon} behavior depended on preparation process. Minimum κ_{phonon} of the MG-HP sample was $1.03 \text{ W m}^{-1} \text{ K}^{-1}$ when milled at 150 rpm and average grain size was $0.47 \mu\text{m}$. Minimum κ_{phonon} of the MA-HP sample was $1.36 \text{ W m}^{-1} \text{ K}^{-1}$ when milled at 120 rpm and average grain size was $0.52 \mu\text{m}$. The effect of grain sizes included fine grain as shown in **Fig. 3.2.3** and microstrain considered by FWHM in **Fig. 3.2.6** confirmed that over 120 rpm, the κ_{phonon} of MG was lower than the κ_{phonon} of MA.

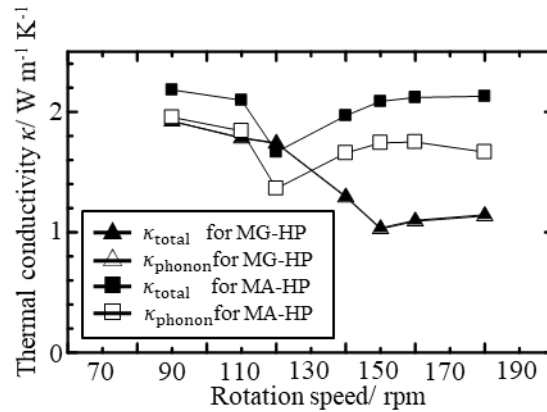


Fig. 3.2.10 Total thermal conductivity κ_{total} and phonon thermal conductivities κ_{phonon} at room temperature and milling rotation speed related to PbTe samples prepared by MG-HP and MA-HP.

The κ_{phonon} values for the PbTe samples prepared by MG-HP and MA-HP at a rotation speed of 90 rpm were fairly close. Samples with a grains of average size over $1 \mu\text{m}$ ($1.47\text{-}1.93 \mu\text{m}$) were correspond to the theoretical calculation of grain boundary scattering [50, 51]. The κ_{phonon} of MG-HP samples tended to decrease with increasing rotational speed because of decreased grain size and the effect of fine grain increased

the microstrain. Samples produced by MA-HP also decreased the κ_{phonon} with increasing milling rotation speed except for over 120 rpm. At over 120 rpm, κ_{phonon} increased and stabilized because microstrain release and because there was high milling energy with high exothermic reaction heat. κ_{phonon} slightly increased grain growth.

In addition, theoretical calculations based on the grain boundary scattering [50, 51] suggested that at 400 K, the κ_{phonon} of undoped PbTe with the average grain size above 1 μm was constant but sharply decreased at a grain size of about 0.01 μm . Grain size was critical in κ_{phonon} transition. **Figure. 3.2.11** shows that the trend of κ_{phonon} at room temperature depend on grain size for samples prepared by MG-HP and MA-HP. This trend was similar to theoretical calculations. κ_{phonon} was significantly changed at around 1 μm . It was different from theoretical calculations based on the grain boundary scattering [50, 51].

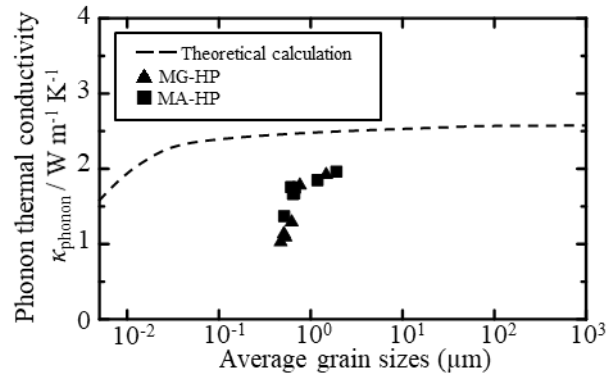


Fig. 3.2.11 Phonon thermal conductivity κ_{phonon} at room temperature and average size of PbTe samples prepared by MG-HP and MA-HP compared with theoretical calculation at 400 K [50, 51].

Figure. 3.2.12 shows the κ_{phonon} at room temperature of PbTe samples with only grain size value at or below 1 μm prepared by MG-HP and MA-HP. Grain sizes over 1 μm were not considered because of the effect of grain boundary scattering on theoretical

calculations [50, 51]. High microstrain led to decrease in κ_{phonon} . Moreover, decrease or increase of κ_{phonon} did not depend on the use of MG or MA. High microstrain decreased κ_{phonon} at grain size at or below 1 μm .

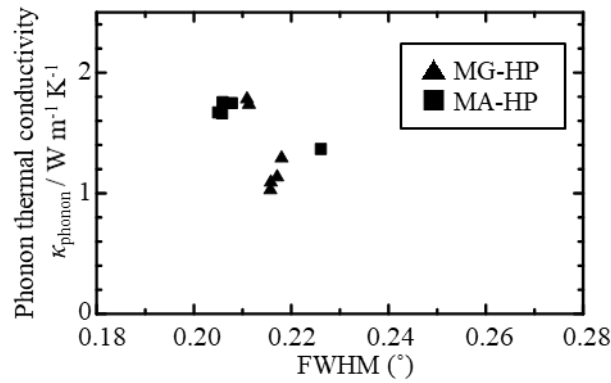


Fig. 3.2.12 Phonon thermal conductivity κ_{phonon} at room temperature with grain size value at or below 1 μm and full width at half maximum (FWHM) fixed on (200) peaks related to PbTe samples prepared by MG-HP and MA-HP.

Therefore, it should be noted here that MG-HP produced finer grain and lower κ_{phonon} than MA-HP. Undoped PbTe samples produced by MG-HP had fine grain and microstrain with high Seebeck coefficient, low κ_{phonon} and low electrical conductivity. Melting process including MG-HP is necessary for preparing these specific experimental conditions.

3.2 BiSbTe results and discussion of “Synthesis and characterization of thermoelectric properties of *p*-type $\text{Bi}_{0.3}\text{Sb}_{1.7}\text{Te}_{3.0}$, prepared by a mechanical alloying (MA) followed by hot pressing with a YSZ ceramics vessel and balls”.

$\text{Bi}_{0.3}\text{Sb}_{1.7}\text{Te}_{3.0}$ powder was prepared by YSZ vessel and balls at various rotation speed.

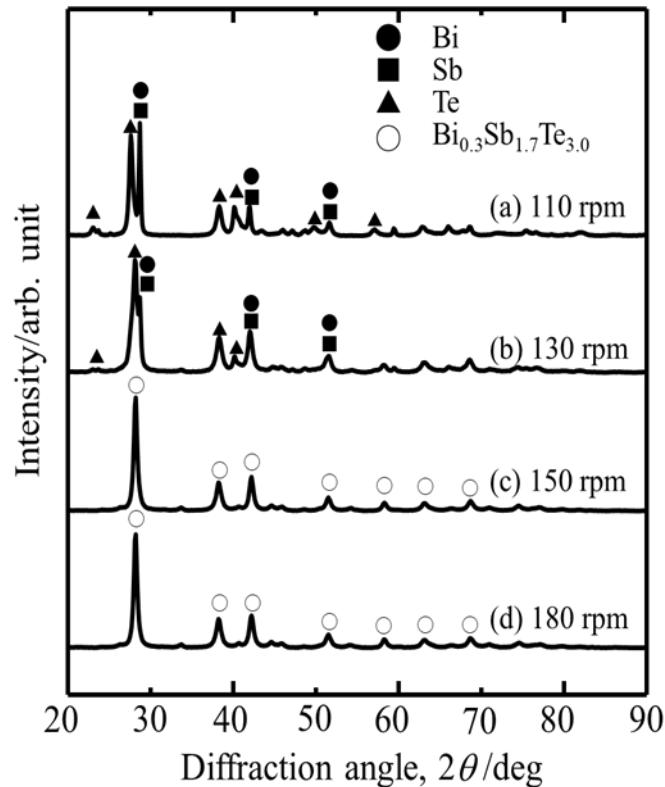


Figure 3.3.1 XRD patterns of milled $\text{Bi}_{0.3}\text{Sb}_{1.7}\text{Te}_{3.0}$ powder. Solid circles, squares, triangles, and open circles represent Bi, Sb, and Te elements, and $\text{Bi}_{0.3}\text{Sb}_{1.7}\text{Te}_{3.0}$ compound, respectively [77].

Milled $\text{Bi}_{0.3}\text{Sb}_{1.7}\text{Te}_{3.0}$ powder as passed through a 150 μm diameter sieve. No material remained on the polymer mesh sieve. **Figure. 3.3.1** shows a sequence of XRD patterns for milled $\text{Bi}_{0.3}\text{Sb}_{1.7}\text{Te}_{3.0}$ powders. XRD patterns of the milled powders showed only peaks of Bi, Sb, Te, and $\text{Bi}_{0.3}\text{Sb}_{1.7}\text{Te}_{3.0}$ [77]. There were no peaks observed from other materials. Powder milled at rotation speed equal to or greater than 150 rpm were completely alloyed and a single phase of $\text{Bi}_{0.3}\text{Sb}_{1.7}\text{Te}_{3.0}$ was obtained. The threshold milling speed for achieving complete alloying in the present study was the same as in

the previous study by stainless-steel vessel and Si_3N_4 balls [68]. The threshold of mechanical alloying was not dependent on the particle size, milling vessel and ball materials, but it depended on milling energy. The milling kinetic energy is proportional to the velocity and mass ratio. At 150 rpm, $\text{Bi}_{0.3}\text{Sb}_{1.7}\text{Te}_{3.0}$ powder became a single-phase, which was used to clarify the homogeneously synthesized materials by ball milling and effects of hot-pressing sintering temperature.

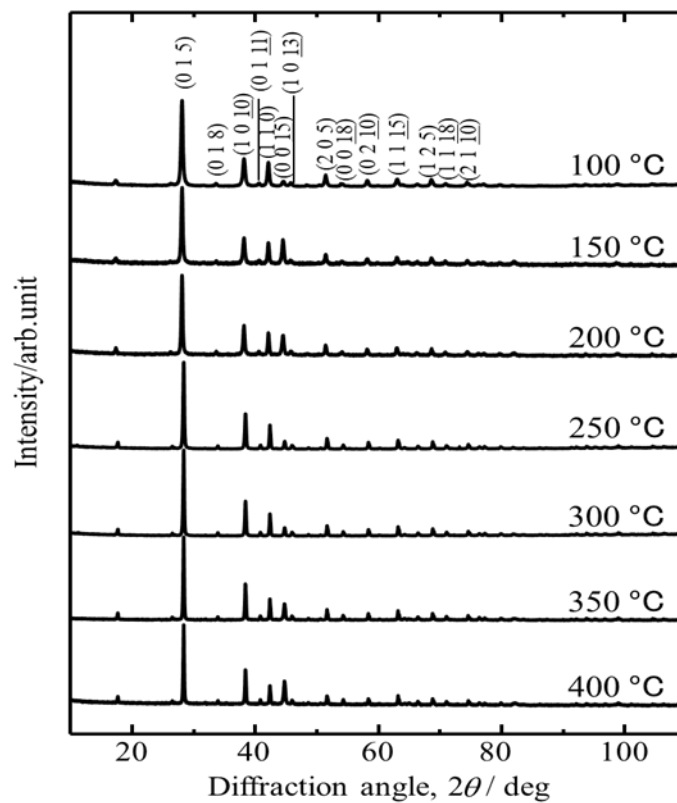


Figure 3.3.2 XRD patterns of $\text{Bi}_{0.3}\text{Sb}_{1.7}\text{Te}_{3.0}$ disks sintered at 100 - 400 °C and milled at 150 rpm; main hkl indexes of $\text{Bi}_{0.3}\text{Sb}_{1.7}\text{Te}_{3.0}$ are shown [77].

Optimum sintering temperature of $\text{Bi}_{0.3}\text{Sb}_{1.7}\text{Te}_{3.0}$ powder milled at minimum rotation speed was needed for complete alloying.

The p -type semiconductors appeared for samples sintered at 100-400 °C. **Figure. 3.3.2** shows a sequence of XRD patterns for $\text{Bi}_{0.3}\text{Sb}_{1.7}\text{Te}_{3.0}$ disks sintered at 100-400 °C and milled at 150 rpm; also, the main hkl indexes of $\text{Bi}_{0.3}\text{Sb}_{1.7}\text{Te}_{3.0}$ [77]. There were no

peaks observed from other materials. XRD pattern peaks show that $\text{Bi}_{0.3}\text{Sb}_{1.7}\text{Te}_{3.0}$ samples had single phase.

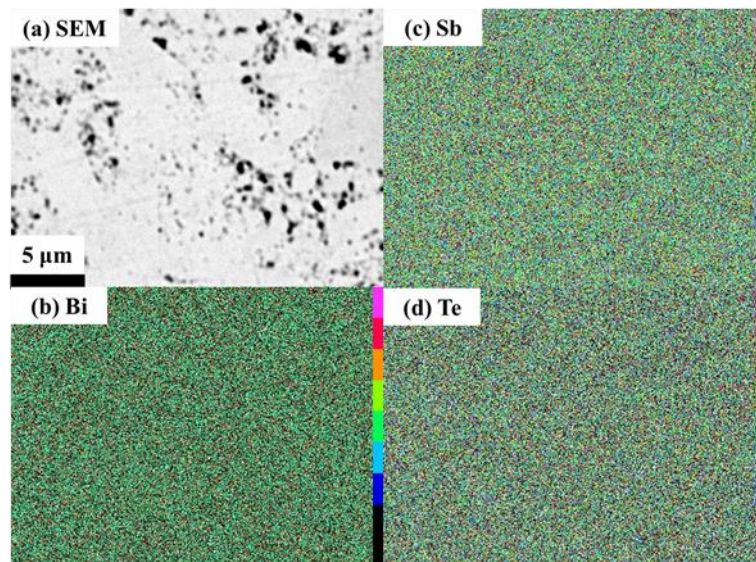


Figure 3.3.3 a) SEM micrograph and b) Bi, c) Sb, and d) Te EDS-derived elemental distributions for $\text{Bi}_{0.3}\text{Sb}_{1.7}\text{Te}_{3.0}$ disk sintered at 100 °C with milling at 150 rpm.

Figure. 3.3.3 (a) shows SEM micrograph of a $\text{Bi}_{0.3}\text{Sb}_{1.7}\text{Te}_{3.0}$ disk sintered at 100 °C and milled at 150 rpm, there were voids and pores. **Figure. 3.3.3 (b), (c), and (d)** show the elemental distributions of Bi, Sb, and Te, respectively, observed by EDS. They were homogeneously dispersed in the observed sample.

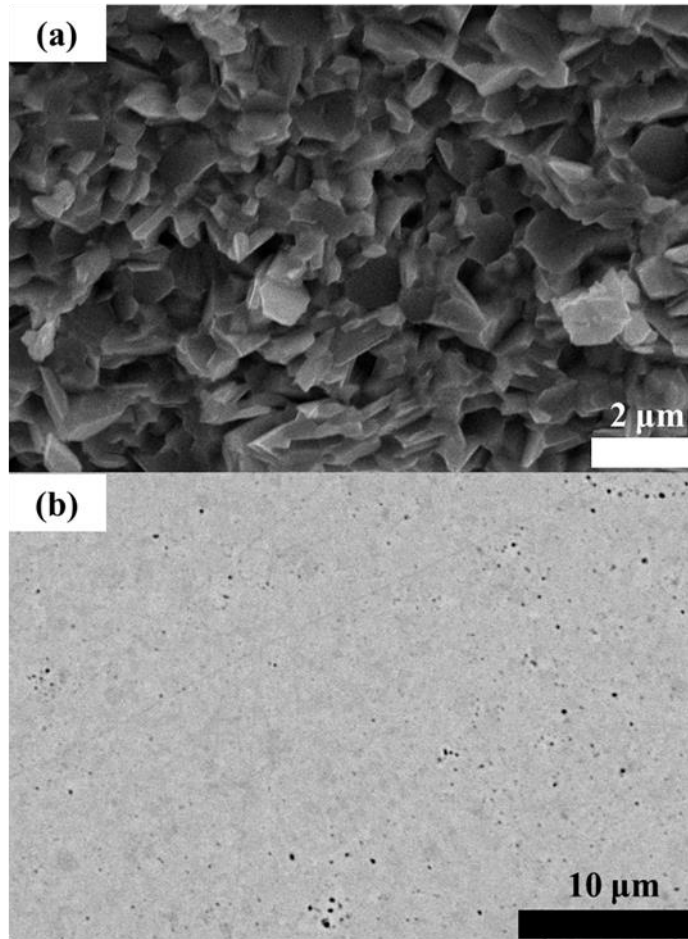


Figure 3.3.4 SEM micrographs of a) fracture surface and b) a cross section of $\text{Bi}_{0.3}\text{Sb}_{1.7}\text{Te}_{3.0}$ disk sintered at 350 °C with milling at 150 rpm.

Figure. 3.3.4 (a) and **(b)** show SEM micrographs of fracture surface and a cross section for $\text{Bi}_{0.3}\text{Sb}_{1.7}\text{Te}_{3.0}$ disk sintered at 350 °C and milled at 150 rpm. $\text{Bi}_{0.3}\text{Sb}_{1.7}\text{Te}_{3.0}$ disk has fine grains and dense. Grain size is approximately 1 μm at the fracture surface. It is similar to that of the previous study [78]. This SEM micrograph confirmed that contaminants from the milling process did not affect matrix grain growth [68].

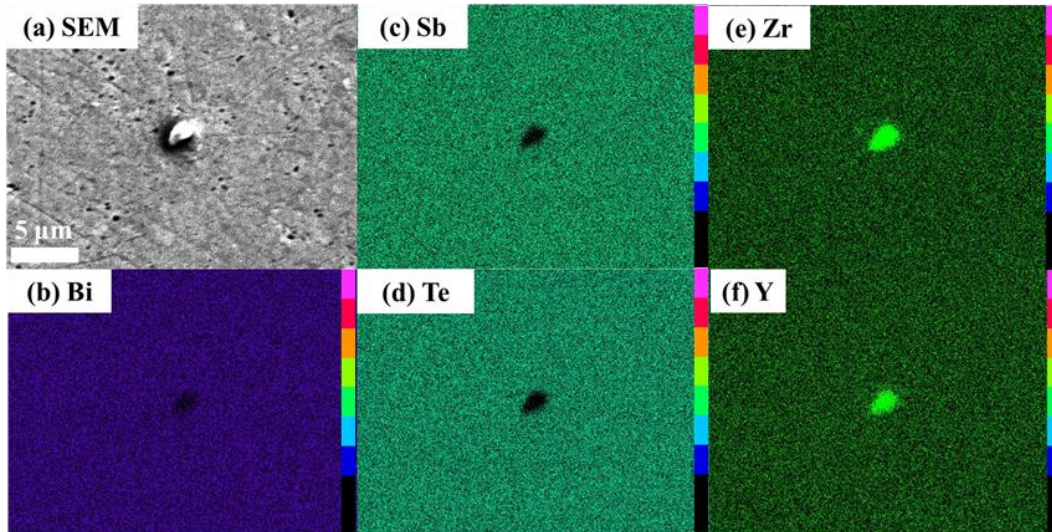


Figure 3.3.5 (a) SEM micrograph and (b) Bi, (c) Sb, (d) Te, (e) Zr, and (f) Y EDS-derived elemental distributions for $\text{Bi}_{0.3}\text{Sb}_{1.7}\text{Te}_{3.0}$ disk sintered at 350 °C with milling at 150 rpm.

Figure. 3.3.5 (a) shows SEM micrographs of a $\text{Bi}_{0.3}\text{Sb}_{1.7}\text{Te}_{3.0}$ disk sintered at 350 °C and milled at 150 rpm. **Figure. 3.3.5 (b)–(f)** show elemental distributions of Bi, Sb, Te, Zr, and Y, respectively, observed by EDS. **Figure. 3.3.5 (a)** shows that the degree of sintering was greater than that in **Figure. 3.3.3 (a)**, Microstructure was dense and similar to that in **Figure. 3.3.4**. Particles of size several micrometers can be observed in the matrix. **Figure. 3.3.5 (e)** and **(f)** indicated that the particles correspond to YSZ. The milling process did not react with $\text{Bi}_{0.3}\text{Sb}_{1.7}\text{Te}_{3.0}$ because a reaction layer between vessel and material did not appear. Relative density of $\text{Bi}_{0.3}\text{Sb}_{1.7}\text{Te}_{3.0}$ disks sintered at 100 and 350 °C and milled at 150 rpm were 95.5% and 99.2%, as calculated based on absolute density of 6.73 g/ cm³ [77]. Relative density increased when increasing heat passed sintering temperature and became denser. They agreed with the SEM micrographs in **Figures. 3.3.3(a)** and **3.3.4(a)**.

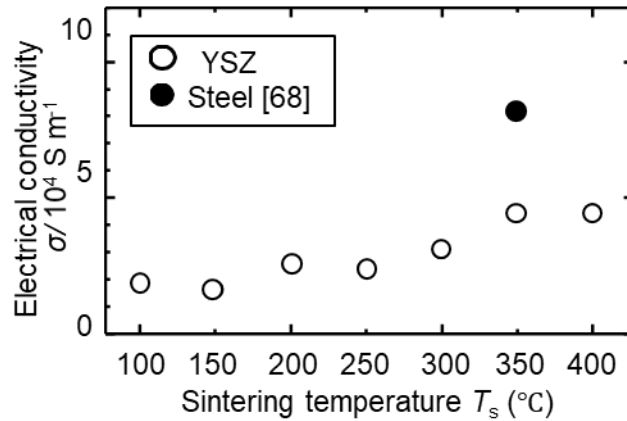


Figure 3.3.6 Electrical conductivity at room temperature and sintering temperature for $\text{Bi}_{0.3}\text{Sb}_{1.7}\text{Te}_{3.0}$ disks milled at 150 rpm.

Figure. 3.3.6 shows electrical conductivity at room temperature and sintering temperature for $\text{Bi}_{0.3}\text{Sb}_{1.7}\text{Te}_{3.0}$ disks milled at 150 rpm. The solid circle shows the electrical conductivity for $\text{Bi}_{0.3}\text{Sb}_{1.7}\text{Te}_{3.0}$ disk sintered at 350 °C, milled at 150 rpm by stainless-steel vessel and Si_3N_4 balls [68]. Sample sintered at 350 °C had a maximum electrical conductivity and increased with increasing sintering temperature. Because the sintering of $\text{Bi}_{0.3}\text{Sb}_{1.7}\text{Te}_{3.0}$ was complete (see in **Figures. 3.3.3 (a)** and **3.3.4 (a)**). Electrical conductivity of samples produced by YSZ vessel and balls had lower than that of samples produced by stainless-steel vessel and Si_3N_4 balls because contamination from stainless steel vessel acted as carrier dopants. Anywise, **Figure. 3.3.5 (a)** shows the presence of YSZ particles of several microscale size in the matrix, but contamination by the YSZ vessel and balls did not have harmful effect to electrical conductivity.

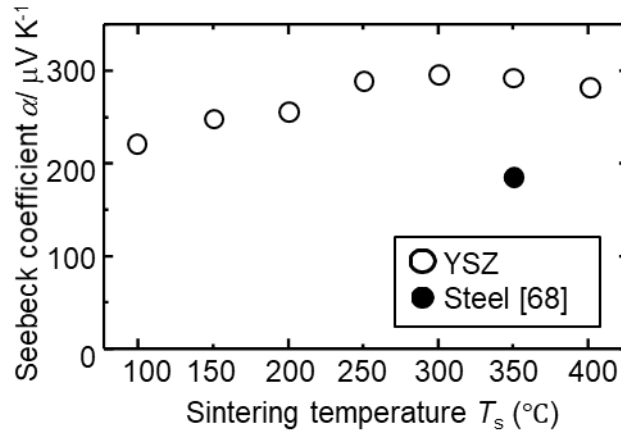


Figure 3.3.7 Seebeck coefficient at room temperature and sintering temperature for $\text{Bi}_{0.3}\text{Sb}_{1.7}\text{Te}_{3.0}$ disks milled at 150 rpm.

Figure. 3.3.7 shows Seebeck coefficient at room temperature and sintering temperature for $\text{Bi}_{0.3}\text{Sb}_{1.7}\text{Te}_{3.0}$ disks milled at 150 rpm. The solid circle shows the Seebeck coefficient for $\text{Bi}_{0.3}\text{Sb}_{1.7}\text{Te}_{3.0}$ disk sintered at 350 °C, milled at 150 rpm by a stainless-steel vessel and Si_3N_4 balls [68]. Sample sintered at 250 °C had a maximum Seebeck coefficient and increased with increasing sintering temperature. Because the sintering of $\text{Bi}_{0.3}\text{Sb}_{1.7}\text{Te}_{3.0}$ was complete (see in **Figures. 3.3.3 (a)** and **3.3.4 (a)**). Seebeck coefficient of samples produced by YSZ vessel and balls were higher than that of samples produced by stainless-steel vessel and Si_3N_4 balls because contamination from stainless steel vessel acted as carrier dopants. On the other hand, contaminants from the YSZ vessel and balls by the milling process did not affect Seebeck coefficients. The inverse relationship between the electrical conductivity and the Seebeck coefficient is consistent with the dependencies on the concentration of free carriers. The observation that low electrical conductivity and high Seebeck coefficients were achieved with YSZ milling shows that contamination was suppressed. Thus, contaminants did not act as carrier dopants in the present study.

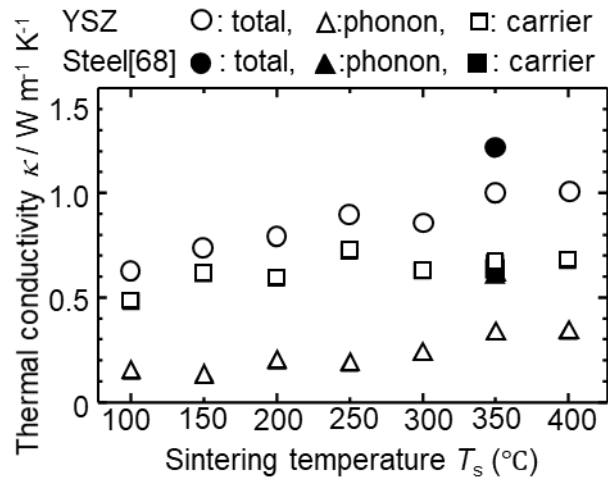


Figure 3.3.8 Total, phonon, and carrier thermal conductivity at room temperature and sintering temperature for $Bi_{0.3}Sb_{1.7}Te_{3.0}$ disks milled at 150 rpm.

Figure. 3.3.8 shows total, phonon, and carrier thermal conductivities at room temperature and sintering temperatures for $Bi_{0.3}Sb_{1.7}Te_{3.0}$ disks milled at 150 rpm. The solid symbols show the values for $Bi_{0.3}Sb_{1.7}Te_{3.0}$ disk sintered at 350 °C, milled at 150 rpm by a stainless-steel vessel and Si_3N_4 balls [68]. Phonon and carrier thermal conductivity were calculated based on equation (2). Sample sintered at 350 °C had a maximum thermal conductivity because sintering was complete. Carrier thermal conductivity of samples produced by YSZ vessel and balls were lower than that of samples produced by stainless-steel vessel and Si_3N_4 balls because contamination from stainless steel vessel acted as carrier dopants. On the other hand, the phonon thermal conductivity was not affected by this milling process and were similar to each other. There is consistency with matrix grain growth being unaffected by the milling vessel (see in **Figure. 3.3.4.**)

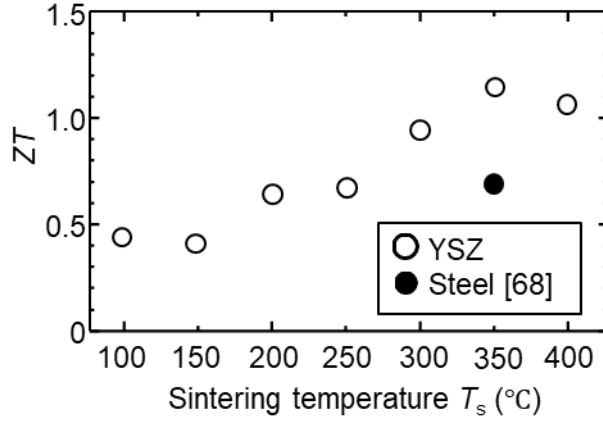


Figure 3.3.9 Dimensionless figure of merit ZT at room temperature and sintering temperature for $\text{Bi}_{0.3}\text{Sb}_{1.7}\text{Te}_{3.0}$ disks milled at 150 rpm.

Figure 3.3.9 shows ZT at room temperature and the sintering temperature for $\text{Bi}_{0.3}\text{Sb}_{1.7}\text{Te}_{3.0}$ disks milled at 150 rpm. The solid circle show the ZT for $\text{Bi}_{0.3}\text{Sb}_{1.7}\text{Te}_{3.0}$ disk sintered at 350 °C, milled at 150 rpm by stainless steel vessel and Si_3N_4 balls [68]. At room temperature, maximum ZT , i.e., 1.14 (α : 292 $\mu\text{V K}^{-1}$, σ : $4.41 \times 10^4 \text{ S m}^{-1}$, κ : 0.99 $\text{W m}^{-1} \text{ K}^{-1}$), was achieved with the disk sintered at 350 °C. ZT values for samples prepared by milling at 150 rpm with a YSZ vessel and balls followed by sintering at 350 °C were enhanced by approximately 1.7 times than that of sample produced by stainless-steel vessel and Si_3N_4 balls. However, in **Fig. 3.3.5**, YSZ particles of size several micrometers were present in the matrix.

These considerations show how the milling process with YSZ can improve ZT . Thermoelectric properties of sintered $\text{Bi}_{0.3}\text{Sb}_{1.7}\text{Te}_{3.0}$ produced by YSZ vessel and balls, at fixed rotation speed and sintering temperature of 350 °C gave the maximum ZT value.

Optimum milling speed and temperature to achieve a maximum ZT value for $\text{Bi}_{0.3}\text{Sb}_{1.7}\text{Te}_{3.0}$.

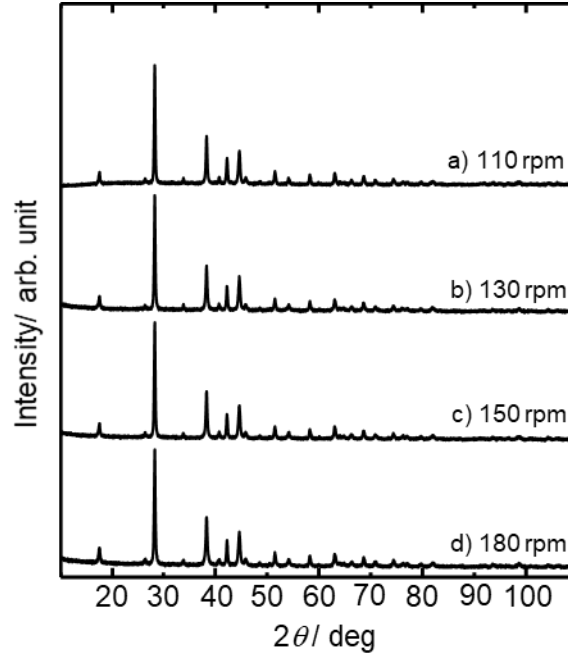


Figure 3.3.10 XRD patterns for disks sintered at 350 °C and milled at 110–180 rpm; main hkl indexes of $\text{Bi}_{0.3}\text{Sb}_{1.7}\text{Te}_{3.0}$ are shown [77].

p -type semiconductors of $\text{Bi}_{0.3}\text{Sb}_{1.7}\text{Te}_{3.0}$ appeared for sample sintered at 350 °C. **Figure. 3.3.10** shows a sequence of XRD patterns for $\text{Bi}_{0.3}\text{Sb}_{1.7}\text{Te}_{3.0}$ milled at 110–180 rpm, and sintered at 350 °C; also, the main hkl indexes of $\text{Bi}_{0.3}\text{Sb}_{1.7}\text{Te}_{3.0}$ are shown [77]. Only peaks from $\text{Bi}_{0.3}\text{Sb}_{1.7}\text{Te}_{3.0}$ are present; no peaks from other materials were observed. Samples were a single-phase of $\text{Bi}_{0.3}\text{Sb}_{1.7}\text{Te}_{3.0}$. The remaining unalloyed materials during milling performed at or below 130 rpm (see **Figure. 3.3.1**) disappeared and materials were formed during subsequent sintering. $\text{Bi}_{0.3}\text{Sb}_{1.7}\text{Te}_{3.0}$ after the milling process was completely alloyed by hot pressing. [68].

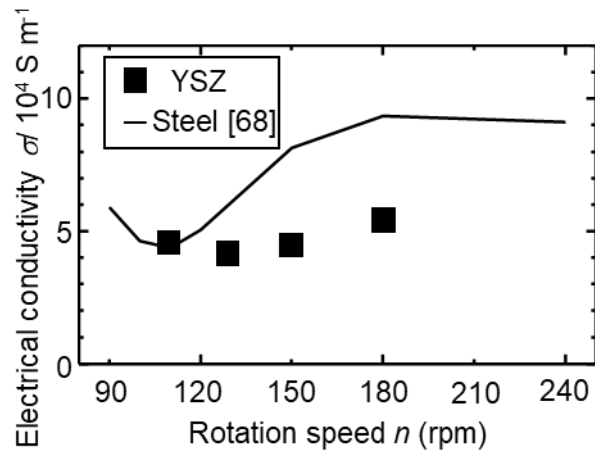


Figure 3.3.11 Electrical conductivity at room temperature and rotation speed for $\text{Bi}_{0.3}\text{Sb}_{1.7}\text{Te}_{3.0}$ disks sintered at 350°C .

Figure 3.3.11 shows electrical conductivity at room temperature and mill rotation speeds for $\text{Bi}_{0.3}\text{Sb}_{1.7}\text{Te}_{3.0}$ disks sintered at 350°C . The solid line shows the value for $\text{Bi}_{0.3}\text{Sb}_{1.7}\text{Te}_{3.0}$ disks sintered at 350°C , milled by stainless-steel vessel and Si_3N_4 balls [68]. At 350°C , electrical conductivities were constant up to 150 rpm and increased at 180 rpm. Because contaminants from milling vessel and balls affected the electrical conductivity, especially at high rotation speed for samples produced by stainless-steel vessel and ball. Electrical conductivities of $\text{Bi}_{0.3}\text{Sb}_{1.7}\text{Te}_{3.0}$ milled with a YSZ vessel were constant up to 150 rpm and then increased slightly at 180 rpm because at high rotation speed, the milling vessel interior is heated by high-energy milling. During the milling process, the heat from inside is released to the outside of vessel via conduction by the vessel material. Thermal conductivity of YSZ and stainless steel are approximately 3 and $16 \text{ W m}^{-1} \text{ K}^{-1}$, respectively [79, 80]. Thus, the heat in a YSZ vessel during the milling process might be more insulated than in a stainless-steel vessel. YSZ milling produced more inside temperature than stainless-steel vessel. At 350°C , vapor pressures of Bi, Sb, and Te were approximately 1×10^{-5} , 1×10^{-4} , and 0.3 Pa, respectively [81]. At

180 rpm, evacuation of Te would therefore occur, which would lead to a Te deficiency in $\text{Bi}_{0.3}\text{Sb}_{1.7}\text{Te}_{3.0}$. Te deficiency created during high-energy YSZ milling leads to decrease in Seebeck coefficient and increase in electrical conductivity of $\text{Bi}_{0.3}\text{Sb}_{1.7}\text{Te}_{3.0+x}$ [78].

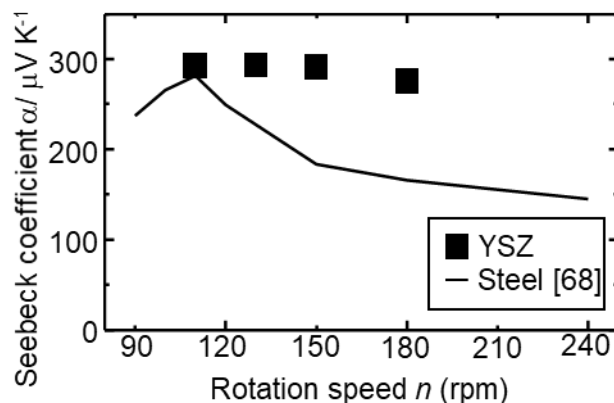


Figure 3.3.12 Seebeck coefficient at room temperature and rotation speed for $\text{Bi}_{0.3}\text{Sb}_{1.7}\text{Te}_{3.0}$ disks sintered at 350 °C.

Figure 3.3.12 shows Seebeck coefficient at room temperature and mill rotation speeds for $\text{Bi}_{0.3}\text{Sb}_{1.7}\text{Te}_{3.0}$ disks sintered at 350 °C and milled with a YSZ vessel and ball. The solid line shows the value for $\text{Bi}_{0.3}\text{Sb}_{1.7}\text{Te}_{3.0}$ disks sintered at 350 °C and milled with a stainless-steel vessel and Si_3N_4 balls [68]. Generally, contamination by the milling vessel increased with increasing rotation speed because of the increased milling energy, but YSZ milling suppressed contamination by materials that acted as carrier dopants. At 180 rpm, Seebeck coefficient for samples produced by YSZ vessel and balls slightly decreased. The reason is the same as the consideration of the effect on electrical conductivity, that is at 180 rpm (high rotation speed), Te evacuation during milling causes a Te deficiency in milled samples.

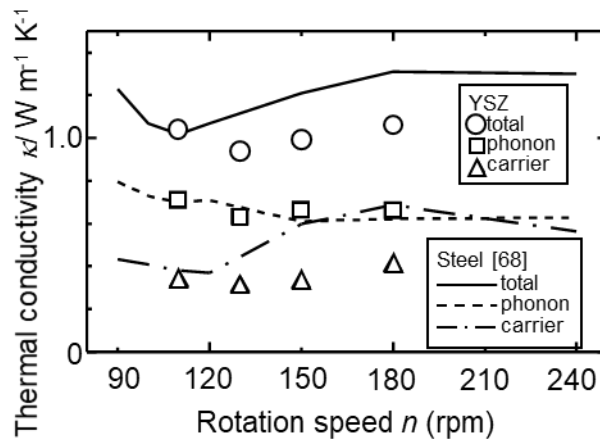


Figure 3.3.13 Total, phonon, and carrier thermal conductivity at room temperature and rotation speed for $\text{Bi}_{0.3}\text{Sb}_{1.7}\text{Te}_{3.0}$ disks sintered at $350\text{ }^\circ\text{C}$ and milled with YSZ vessel and ball (open symbols). Total, phonon, and carrier thermal conductivity of $\text{Bi}_{0.3}\text{Sb}_{1.7}\text{Te}_{3.0}$ disks sintered at $350\text{ }^\circ\text{C}$ and milled at 150 rpm with stainless-steel vessel and Si_3N_4 balls are shown by solid, dashed, and alternating long and short dashed lines, respectively [68].

Figure. 3.3.13 shows total, phonon, and carrier thermal conductivities at room temperature and mill rotation speeds for $\text{Bi}_{0.3}\text{Sb}_{1.7}\text{Te}_{3.0}$ disks sintered at $350\text{ }^\circ\text{C}$ and milled with a YSZ vessel and balls. Also, total, phonon, and carrier thermal conductivity of $\text{Bi}_{0.3}\text{Sb}_{1.7}\text{Te}_{3.0}$ disks sintered at $350\text{ }^\circ\text{C}$ and milled with a stainless-steel vessel and Si_3N_4 balls are presented [68]. The difference between carrier thermal conductivity leads to the difference in total thermal conductivity for samples milled with YSZ vessel and balls and those of samples milled with a stainless-steel vessel and Si_3N_4 balls. Carrier thermal conductivities for sample produced by YSZ vessel and balls were constant up to 150 rpm and then increased slightly at 180 rpm. There is consistency with the effects of milling on the electrical conductivity and Seebeck coefficients, which are caused by suppression of contaminants that act as carrier dopants, and creation of a Te deficiency [78]. Phonon thermal conductivities of samples milled with a YSZ vessel and balls were constant and similar to those of samples milled with a stainless-steel vessel

and Si_3N_4 balls and were not affected by contamination from YSZ vessel and balls.

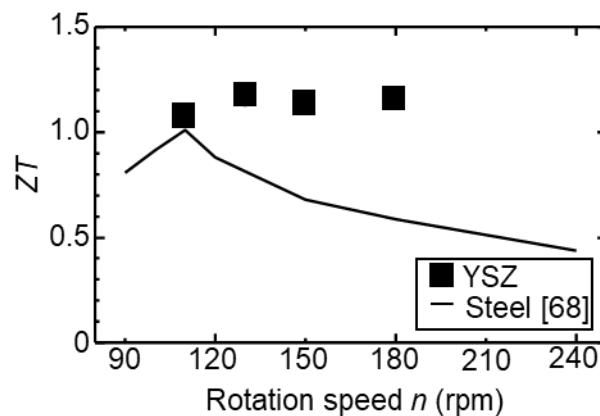


Figure 3.3.14 Dimensionless figure of merit ZT at room temperature and rotation speed for $\text{Bi}_{0.3}\text{Sb}_{1.7}\text{Te}_{3.0}$ disks sintered at $350\text{ }^\circ\text{C}$.

Figure 3.3.14 shows ZT at room temperature and mill rotation speeds for $\text{Bi}_{0.3}\text{Sb}_{1.7}\text{Te}_{3.0}$ disks sintered at $350\text{ }^\circ\text{C}$. The solid line shows the values for $\text{Bi}_{0.3}\text{Sb}_{1.7}\text{Te}_{3.0}$ disks sintered at $350\text{ }^\circ\text{C}$ and milled with a stainless-steel vessel and Si_3N_4 balls [68]. ZT values for samples produced by YSZ vessel were constant, but different when compared with samples produced by stainless-steel vessel and Si_3N_4 balls. At 130 rpm, contaminants from the YSZ vessel and milling balls improved the ZT value at room temperature, and remained above 1.0 and reached a peak of 1.16 (α : $295\text{ }\mu\text{V K}^{-1}$, σ : $4.16 \times 10^4\text{ S m}^{-1}$, κ : $0.94\text{ W m}^{-1}\text{ K}^{-1}$). These results confirmed that samples produced by YSZ vessel and balls improved the ZT because it suppressed contamination by materials that acted as carrier dopants for $\text{Bi}_{0.3}\text{Sb}_{1.7}\text{Te}_{3.0}$. The improvements in the thermoelectric properties are strongly affected by the milling vessel and ball materials.

CHAPTER 4

CONCLUSIONS

4.1 Lead telluride (PbTe) research conclusions

4.1.1 The present study investigated the thermoelectric properties of undoped PbTe prepared by Melting-HP and BM-HP at various rotation speed using planetary ball milling. The results can be summarized as follows.

1. XRD patterns indicated that planetary ball milling produces single-phase PbTe crystal structure. The obtained PbTe samples were dense and had relative density greater than 99%.
2. Average grain sizes of Melting-HP and BM-HP samples milled at 90, 120, 150 and 180 rpm were 22.62, 1.15, 0.80, 0.72, and 0.66 μm , respectively. Average grain size decreased and became fine as increasing rotation speed. Thermal conductivity was lowest when rotation speed reached 120 rpm.
3. PbTe produced by Melting-HP had average grain size of 22.62 μm and κ_{phonon} value of 2.20 $\text{W m}^{-1} \text{K}^{-1}$. PbTe produced by BM-HP at 120 rpm had average grain size of 0.80 μm and κ_{phonon} value of 1.29 $\text{W m}^{-1} \text{K}^{-1}$. The κ_{phonon} value of PbTe produced by BM-HP at 120 rpm was lower than in PbTe produced by Melting-HP. Because average grain size was below 1 μm . There was a significant inverse relationship between κ_{phonon} and FWHM. The low κ_{phonon} was associated with fine grain and high internal strain.
4. The decreasing behavior between κ_{phonon} and average grain size agreed with theoretical calculation by grain boundary scattering. The observed critical point around 1 μm differed from theoretical calculation by grain boundary scattering.

These experimental results for the behavior of κ_{phonon} and average grain size are in agreement with theoretical calculations.

4.1.2 The thermoelectric properties of undoped PbTe prepared by MG and MA processes and at various mill rotation speeds, followed by HP were investigated. The results are summarized as follows.

1. Samples prepared by MG-HP and MA-HP were obtained a single-phase. The samples prepared by MG-HP had a high relative density close to 99%. The bulk density of samples prepared by MA-HP was above theoretical value. During the MA process, high exothermic reaction heat between Pb and Te caused Te evaporation, because Te has higher vapor pressure than Pb.

2. Samples prepared by MG-HP showed that microstrain increased continuously and average grain sizes decreased with milling rotation speed. At 150 rpm, minimum κ_{phonon} was $1.03 \text{ W m}^{-1} \text{ K}^{-1}$ and average grain size was $0.47 \text{ }\mu\text{m}$. For samples prepared by MA-HP, at 120 rpm, minimum κ_{phonon} was $1.36 \text{ W m}^{-1} \text{ K}^{-1}$ and average grain size was $0.52 \text{ }\mu\text{m}$. Microstrain released at 140-180 rpm and average grain sizes were slightly higher than that for MG-HP in these rotational ranges. MG-HP produced finer grain and lower κ_{phonon} than MA-HP. The MG process produced kinetic energy while the MA process produced kinetic energy with high exothermic reaction heat, leading to different microstrain and grain size.

3. Because Te deficiency acts as dopant, electrical conductivity and Seebeck coefficient in MA-HP samples behaved like *p*-type doped materials.

4. κ_{phonon} of grain size over $1 \text{ }\mu\text{m}$ agreed with theoretical calculation of grain boundary scattering. Reduction of κ_{phonon} for grain sizes below $1 \text{ }\mu\text{m}$ increased with microstrain.

Reduction of κ_{phonon} in thermoelectric materials prepared by milling processes affected fine grain and microstrain caused by high exothermic reaction heat not only for PbTe but also for other thermoelectric materials as well.

4.2 Bismuth antimony telluride (BiSbTe) research conclusions

p-type Bi_{0.3}Sb_{1.7}Te_{3.0} were prepared by a MA–HP process and at various rotation speeds with YSZ vessel and balls. The results are summarized as follows.

1. Powders milled at rotation speeds equal to or greater than 150 rpm were completely alloyed and given a single-phase. The threshold milling speed for complete alloying prepared by YSZ vessel and balls was the same as that of milling with a stainless-steel vessel and Si₃N₄ balls.

2. At 350 °C, the sintered sample had 1 μm grain size at the fracture surface. The attrition of the milling vessel and balls was not detrimental to the matrix grain growth at given milling ball-to-material weight ratio and milling speed.

3. Samples produced by YSZ vessel and balls had higher Seebeck coefficients and lower electrical conductivity than in the case of samples produced by stainless-steel vessel and Si₃N₄ balls. YSZ milling suppressed contamination by materials that acted as carrier dopants.

4. At 150 rpm, *ZT* values for samples produced by YSZ vessel and balls followed by hot pressing sintered at 350 °C was enhanced approximately by 1.7 times and was higher than the sample produced by stainless-steel vessel and Si₃N₄ balls.

5. At 130 rpm, *ZT* remained above 1.0 and reached a peak of 1.16 (α : 295 μV K⁻¹, σ : 4.16×10⁴ S m⁻¹, κ : 0.94 W m⁻¹ K⁻¹, T : 300 K) for the sample sintered at 350 °C.

These results indicate that milling with a YSZ vessel and balls improves *ZT* by suppressing contamination with materials that act as carrier dopants. Improvements in the Bi_{0.3}Sb_{1.7}Te_{3.0} properties are strongly affected by the milling vessel and ball materials.

References

- [1] H.J. Goldsmid, Introduction to thermoelectricity, Springer, New York, 2010, p. 1-10.
- [2] A. Shakouri, Recent developments in semiconductor thermoelectric physics and materials, Annual review of materials research, 41 (2011) 399-425.
- [3] C.B. Vining, An inconvenient truth about thermoelectrics, Nature materials, 8 (2009) 83-85.
- [4] D. Beretta, N. Neophytou, J.M. Hodges, M.G. Kanatzidis, D. Narducci, M. Martin-Gonzalez, M. Beekman, B. Balke, G. Cerretti, W. Tremel, Thermoelectrics: From history, a window to the future, Materials Science and Engineering: R: Reports, (2018) 1-47.
- [5] K. Hasezaki, M. Nishimura, M. Umata, H. Tsukuda, M. Araoka, Mechanical alloying of BiTe and BiSbTe thermoelectric materials, Materials transactions, JIM, 35 (1994) 428-432.
- [6] J. Fleurial, L. Gailliard, R. Triboulet, H. Scherrer, S. Scherrer, Thermal properties of high quality single crystals of bismuth telluride—Part I: Experimental characterization, Journal of Physics and Chemistry of Solids, 49 (1988) 1237-1247.
- [7] B. Madavali, H.-S. Kim, K.-H. Lee, Y. Isoda, F. Gascoin, S.-J. Hong, Large scale production of high efficient and robust *p*-type Bi-Sb-Te based thermoelectric materials by powder metallurgy, Materials & Design, 112 (2016) 485-494.
- [8] L. Hicks, M.S. Dresselhaus, Effect of quantum-well structures on the thermoelectric figure of merit, Physical Review B, 47 (1993) 12727.
- [9] Y. Noda, M. Orihashi, I.A. Nishida, Thermoelectric properties of *p*-type lead telluride doped with silver or potassium, Materials Transactions, JIM, 39 (1998) 602-605.

- [10] A. Crocker, L. Rogers, Interpretation of the Hall coefficient, electrical resistivity and Seebeck coefficient of *p*-type lead telluride, *British Journal of Applied Physics*, 18 (1967) 563-573.
- [11] R. Breschi, V. Fano, The sintering of lead telluride, *Journal of Materials science*, 20 (1985) 2990-2996.
- [12] C.B. Vining, A model for the high-temperature transport properties of heavily doped *n*-type silicon-germanium alloys, *Journal of Applied Physics*, 69 (1991) 331-341.
- [13] C.B. Vining, W. Laskow, J.O. Hanson, R.R. Van der Beck, P.D. Gorsuch, Thermoelectric properties of pressure-sintered Si_{0.8}Ge_{0.2} thermoelectric alloys, *Journal of applied physics*, 69 (1991) 4333-4340.
- [14] N. Niizeki, M. Kato, I.J. Ohsugi, Y. Isoda, H. Kohri, I. Shiota, Effect of aluminum and copper addition to the thermoelectric properties of FeSi₂ sintered in the atmosphere, *Materials transactions*, 50 (2009) 1586-1591.
- [15] A.D. LaLonde, Y. Pei, H. Wang, G. Jeffrey Snyder, Lead telluride alloy thermoelectrics, *Materials Today*, 14 (2011) 526-532.
- [16] Y. Pei, A. LaLonde, S. Iwanaga, G.J. Snyder, High thermoelectric figure of merit in heavy hole dominated PbTe, *Energy & Environmental Science*, 4 (2011) 2085-2089.
- [17] Y. Pei, X. Shi, A. LaLonde, H. Wang, L. Chen, G.J. Snyder, Convergence of electronic bands for high performance bulk thermoelectrics, *Nature*, 473 (2011) 66-69.
- [18] C. Wood, Materials for thermoelectric energy conversion, *Reports on progress in physics*, 51 (1988) 459.
- [19] K. Biswas, J. He, I.D. Blum, C.-I. Wu, T.P. Hogan, D.N. Seidman, V.P. Dravid, M.G. Kanatzidis, High-performance bulk thermoelectrics with all-scale hierarchical architectures, *Nature*, 489 (2012) 414-418.

- [20] H. Goldsmid, R. Douglas, The use of semiconductors in thermoelectric refrigeration, *British Journal of Applied Physics*, 5 (1954) 386.
- [21] H.J. Goldsmid, Bismuth telluride and its alloys as materials for thermoelectric generation, *Materials*, 7 (2014) 2577-2592.
- [22] W. Xie, X. Tang, Y. Yan, Q. Zhang, T.M. Tritt, Unique nanostructures and enhanced thermoelectric performance of melt-spun BiSbTe alloys, *Applied Physics Letters*, 94 (2009) 102111.
- [23] B. Poudel, Q. Hao, Y. Ma, Y. Lan, A. Minnich, B. Yu, X. Yan, D. Wang, A. Muto, D. Vashaee, High-thermoelectric performance of nanostructured bismuth antimony telluride bulk alloys, *Science*, 320 (2008) 634-638.
- [24] S.I. Kim, K.H. Lee, H.A. Mun, H.S. Kim, S.W. Hwang, J.W. Roh, D.J. Yang, W.H. Shin, X.S. Li, Y.H. Lee, Dense dislocation arrays embedded in grain boundaries for high-performance bulk thermoelectrics, *Science*, 348 (2015) 109-114.
- [25] A. Soni, Z. Yanyuan, Y. Ligen, M.K.K. Aik, M.S. Dresselhaus, Q. Xiong, Enhanced Thermoelectric Properties of Solution Grown $\text{Bi}_2\text{Te}_{3-x}\text{Se}_x$ Nanoplatelet Composites, *Nano letters*, 12 (2012) 1203-1209.
- [26] K. Hirota, K. Takagi, K. Hanasaku, K.L. Hasezaki, H. Saito, S. Hata, K. Hasezaki, Carbon observation by electron energy-loss spectroscopy and thermoelectric properties of graphite added bismuth antimony telluride prepared by mechanical alloying-hot pressing, *Intermetallics*, 109 (2019) 1-7.
- [27] L. Hu, T. Zhu, X. Liu, X. Zhao, Point defect engineering of high-performance Bismuth-Telluride-based thermoelectric materials, *Advanced Functional Materials*, 24 (2014) 5211-5218.
- [28] C. Han, Q. Sun, Z. Li, S.X. Dou, Thermoelectric enhancement of different kinds of

metal chalcogenides, *Advanced Energy Materials*, 6 (2016) 1600498.

[29] M.G. Kanatzidis, T. Hogan, S. Mahanti, *Chemistry, physics, and materials science of thermoelectric materials: beyond bismuth telluride*, Springer Science & Business Media, New York, 2012, p. 35.

[30] D.M. Rowe, *Thermoelectrics handbook: Macro to Nano, General Principles and Basic Considerations*, CRC press, Taylor& Francis Group, Boca Raton, Florida, 2005, pp. 1-10.

[31] G.J. Snyder, E.S. Toberer, *Complex thermoelectric materials*, in: *Materials For Sustainable Energy: A Collection of Peer-Reviewed Research and Review Articles from Nature Publishing Group*, World Scientific, 2011, pp. 101-110.

[32] H.J. Goldsmid, *The Thermoelectric and Related Effects*, in: *Introduction to thermoelectricity*, Springer, London, 2016, pp. 1-7.

[33] Y. Shinohara, *Recent progress of thermoelectric devices or modules in Japan*, *Materials Today: Proceedings*, 4 (2017) 12333-12342.

[34] T.M. Tritt, *Thermal conductivity: theory, properties, and applications*, Kluwer Academic/ Plenum Publishers, New York, 2004, pp. 1-17.

[35] A.D. LaLonde, Y. Pei, G.J. Snyder, *Reevaluation of $\text{PbTe}_{1-x}\text{I}_x$ as high performance *n*-type thermoelectric material*, *Energy & Environmental Science*, 4 (2011) 2090-2096.

[36] C. Long, X. Hou, Y. Gelbstein, J. Zhang, B. Ren, Z. Wang, *Preparation and Thermoelectric Properties of N-type PbTe Doped with In and PbI_2* , in: *2006 25th International Conference on Thermoelectrics*, 2006, pp. 382-385.

[37] G. Chen, M.S. Dresselhaus, G. Dresselhaus, J.P. Fleurial, T. Caillat, *Recent developments in thermoelectric materials*, *International Materials Reviews*, 48 (2003) 45-66.

- [38] Y. Takagiwa, Y. Pei, G. Pomrehn, G.J. Snyder, Dopants effect on the band structure of PbTe thermoelectric material, *Applied Physics Letters*, 101 (2012) 092102-092103.
- [39] Y. Takagiwa, Y. Pei, G. Pomrehn, G. Jeffrey Snyder, Validity of rigid band approximation of PbTe thermoelectric materials, *APL Materials*, 1 (2013).
- [40] D.R. Lide, *CRC handbook of chemistry and physics: a ready-reference book of chemical and physical data*, CRC press, Taylor& Francis Group, Boca Raton, Florida, 1995, pp. 4-65.
- [41] E. Rogacheva, I. Krivulkin, V. Popov, T. Lobkovskaya, Concentration dependences of properties in $\text{Pb}_{1-x}\text{Mn}_x\text{Te}$ solid solutions, *physica status solidi (a)*, 148 (1995) K65-K67.
- [42] A. Jacquot, B. Lenoir, M. Boffoue, A. Dauscher, Pulsed laser deposition of PbTe films on glass substrates, *Applied Physics A*, 69 (1999) S613-S615.
- [43] Y. Gelbstein, G. Gotesman, Y. Lishzinker, Z. Dashevsky, M.P. Dariel, Mechanical properties of PbTe-based thermoelectric semiconductors, *Scripta Materialia*, 58 (2008) 251-254.
- [44] Y. Gelbstein, $\text{Pb}_{1-x}\text{Sn}_x\text{Te}$ Alloys: Application Considerations, *Journal of electronic materials*, 40 (2011) 533-536.
- [45] J.E. Ni, E.D. Case, K.N. Khabir, R.C. Stewart, C.-I. Wu, T.P. Hogan, E.J. Timm, S.N. Girard, M.G. Kanatzidis, Room temperature Young's modulus, shear modulus, Poisson's ratio and hardness of PbTe–PbS thermoelectric materials, *Materials Science and Engineering: B*, 170 (2010) 58-66.
- [46] Y. Gelbstein, Z. Dashevsky, M. Dariel, Powder metallurgical processing of functionally graded $p\text{-Pb}_{1-x}\text{Sn}_x\text{Te}$ materials for thermoelectric applications, *Physica B: Condensed Matter*, 391 (2007) 256-265.

- [47] N. Bouad, R. Marin-Ayral, J. Tedenac, Mechanical alloying and sintering of lead telluride, *Journal of Alloys and Compounds*, 297 (2000) 312-318.
- [48] N. Bouad, R.M. Marin-Ayral, G. Nabias, J.C. Tédénac, Phase transformation study of Pb–Te powders during mechanical alloying, *Journal of Alloys and Compounds*, 353 (2003) 184-188.
- [49] N. Bouad, L. Chapon, R.M. Marin-Ayral, F. Bouree-Vigneron, J.C. Tedenac, Neutron powder diffraction study of strain and crystallite size in mechanically alloyed PbTe, *Journal of Solid State Chemistry*, 173 (2003) 189-195.
- [50] J. Yoshino, Theoretical estimation of thermoelectric figure of merit in sintered materials and proposal of grain-size-graded structures, in: *Functionally Graded Materials 1996*, Elsevier, 1997, pp. 495-500.
- [51] J. Yoshino, Thermoelectric Energy Conversion, in: S. Makoto (Ed.) *Theory and Application*, Shokabo, Tokyo, 2005, pp. 44-51.
- [52] C. Bhandari, D. Rowe, High-temperature thermal transport in heavily doped small-grain-size lead telluride, *Applied Physics A*, 37 (1985) 175-178.
- [53] R. Hanus, M.T. Agne, A.J. Rettie, Z. Chen, G. Tan, D.Y. Chung, M.G. Kanatzidis, Y. Pei, P.W. Voorhees, G.J. Snyder, Lattice Softening Significantly Reduces Thermal Conductivity and Leads to High Thermoelectric Efficiency, *Advanced Materials*, 31 (2019) 1900108.
- [54] O. Falkenbach, M.O. Loeh, C.W. Wiegand, A. Schmitz, D. Hartung, G. Koch, P.J. Klar, E. Mueller, S. Schlecht, Structural and Thermoelectric Properties of Nanostructured Nominally Stoichiometric $\text{Pb}_{1-x}\text{Bi}_x\text{Te}$ Prepared by Mechanical Alloying, *Journal of Electronic Materials*, 46 (2017) 5781-5791.
- [55] A. Królicka, A. Materna, M. Piersa, A. Mirowska, Impact of Different Conditions

of Technological Process on Thermoelectric Properties of Fine-Grained PbTe, *Acta Physica Polonica A*, 130 (2016) 1255-1258.

[56] Y. Li, D. Mei, H. Wang, Z. Yao, T. Zhu, S. Chen, Reduced lattice thermal conductivity in nanograined Na-doped PbTe alloys by ball milling and semisolid powder processing, *Materials Letters*, 140 (2015) 103-106.

[57] C.-H. Kuo, H.-S. Chien, C.-S. Hwang, Y.-W. Chou, M.-S. Jeng, M. Yoshimura, Thermoelectric Properties of Fine-Grained PbTe Bulk Materials Fabricated by Cryomilling and Spark Plasma Sintering, *Materials Transactions*, 52 (2011) 795-801.

[58] A. Schmitz, C. Stiewe, K. Zabrocki, J. de Boor, K. Mull, E. Müller, Current assisted sintering of PbTe—Effects on thermoelectric and mechanical properties, *Materials Research Bulletin*, 86 (2017) 159-166.

[59] D. Rowe, C. Bhandari, Lattice thermal conductivity of small grain size PbSnTe and PbGeTe thermoelectric material, *Applied Physics Letters*, 47 (1985) 255-257.

[60] C. Bhandari, D. Rowe, The effect of phonon-grain boundary scattering, doping and alloying on the lattice thermal conductivity of lead telluride, *Journal of Physics D: Applied Physics*, 16 (1983) L75-L77.

[61] C.-H. Su, Design, growth and characterization of PbTe-based thermoelectric materials, *Progress in Crystal Growth and Characterization of Materials*, 65 (2019) 47-94.

[62] O. Meroz, D. Ben-Ayoun, O. Beeri, Y. Gelbstein, Development of Bi₂Te_{2.4}Se_{0.6} alloy for thermoelectric power generation applications, *Journal of Alloys and Compounds*, 679 (2016) 196-201.

[63] F.-H. Lin, C.-J. Liu, A simple energy-saving aqueous synthesis of Bi₂Te₃ nanocomposites yielding relatively high thermoelectric power factors, *Ceramics*

International, 45 (2019) 9397-9400.

[64] M. Keshavarz, D. Vasilevskiy, R. Masut, S. Turenne, *p*-Type bismuth telluride-based composite thermoelectric materials produced by mechanical alloying and hot extrusion, *Journal of electronic materials*, 42 (2013) 1429-1435.

[65] Q. Lognoné, F. Gascoin, Reactivity, stability and thermoelectric properties of *n*-Bi₂Te₃ doped with different copper amounts, *Journal of alloys and compounds*, 610 (2014) 1-5.

[66] A. Pakdel, Q. Guo, V. Nicolosi, T. Mori, Enhanced thermoelectric performance of Bi-Sb-Te/Sb₂O₃ nanocomposites by energy filtering effect, *Journal of Materials Chemistry A*, 6 (2018) 21341-21349.

[67] C.C. Koch, J. Whittenberger, Mechanical milling/alloying of intermetallics, *Intermetallics*, 4 (1996) 339-355.

[68] M. Kitamura, K. Hirota, K. Hasezaki, Relationships between Thermoelectric Properties and Milling Rotational Speed on Bi_{0.3}Sb_{1.7}Te_{3.0} Thermoelectric Materials, *Materials Transactions*, 59 (2018) 1225-1232.

[69] A. Sayyadi-Shahraki, S.M. Rafiaei, S. Ghadami, K.A. Nekouee, Densification and mechanical properties of spark plasma sintered Si₃N₄/ZrO₂ nano-composites, *Journal of Alloys and Compounds*, 776 (2019) 798-806.

[70] S. Turenne, T. Clin, D. Vasilevskiy, R. Masut, Finite element thermomechanical modeling of large area thermoelectric generators based on bismuth telluride alloys, *Journal of electronic materials*, 39 (2010) 1926-1933.

[71] J.C. Wurst, J.A. Nelson, Lineal Intercept Technique for Measuring Grain Size in Two-Phase Polycrystalline Ceramics, *Journal of the American Ceramic Society*, 55 (1972) 109-109.

- [72] M. Fusa, N. Yamamoto, K. Hasezaki, Measurement of Seebeck Coefficient and Conductive Behaviors of $\text{Bi}_2\text{Te}_{3-x}\text{Se}_x(x=0.15-0.6)$ Thermoelectric Semiconductors without Harmful Dopants, *Materials Transactions*, 55 (2014) 942-946.
- [73] T. Hamachiyo, M. Ashida, K. Hasezaki, Retraction: Fine Measurement of Thermal Conductivity for $(\text{Bi}_{0.5}\text{Sb}_{1.5})\text{Te}_3$ Compounds, *Materials Transactions*, 50 (2009) 167-170.
- [74] R.F. Bis, Temperature-pressure projection of lead telluride phase diagram, *Journal of Physics and Chemistry of Solids*, 24 (1963) 579-581.
- [75] J. Lin, K. Hsleh, R. Sharma, Y. Chang, The Pb-Te (lead-tellurium) system, *Bulletin of Alloy Phase Diagrams*, 10 (1989) 340-347.
- [76] J.C. Lin, K.C. Hsleh, R.C. Sharma, Y.A. Chang, The Pb-Te (lead-tellurium) system, *Bulletin of Alloy Phase Diagrams*, 10 (1989) 340-347.
- [77] C. Chen, B. Zhang, D. Liu, Z. Ge, Thermoelectric properties of $\text{Cu}_y\text{Bi}_x\text{Sb}_{2-x-y}\text{Te}_3$ alloys fabricated by mechanical alloying and spark plasma sintering, *Intermetallics*, 25 (2012) 131-135.
- [78] K. Hirota, M. Kitamura, K. Takagi, K. Hasezaki, Thermoelectric Behaviors of $\text{Bi}_{0.3}\text{Sb}_{1.7}\text{Te}_{3.0}$ with Excess or Deficiency of Tellurium Prepared by Mechanical Alloying Followed by Hot Pressing, *Materials Transactions*, 59 (2018) 1233-1238.
- [79] K. Schlichting, N. Padture, P. Klemens, Thermal conductivity of dense and porous yttria-stabilized zirconia, *Journal of materials science*, 36 (2001) 3003-3010.
- [80] D. Benjamin, C.W. Kirkpatrick, Properties and selection: stainless steels, tool materials and special purpose metals, ASM International (OH), 1980, pp. 34-35.
- [81] E.R. Cohen, D.R. Lide, G.L. Trigg, AIP physics desk reference, 3 ed., Springer-Verlag, New York, 2003, pp. 831-833.

LIST OF PUBLICATIONS

This work of this thesis based on the following publications:

1. M. Bumrungpon, K. Hirota, K. Takagi, K. Hanasaku, T. Hirai, I. Morioka, R. Yasufuku, M. Kitamura, K. Hasezaki, Synthesis and thermoelectric properties of bismuth antimony telluride thermoelectric materials fabricated at various ball-milling speeds with yttria-stabilized zirconia ceramic vessel and balls, *Ceramics International*, (2020) 13869-13876. [doi.org/10.1016/j.ceramint.2020.02.180].
2. M. Bumrungpon, I. Morioka, R. Yasufuku, T. Hirai, K. Hanasaku, K. Hirota, K. Takagi and K. Hasezaki, The Critical Point of Average Grain Size in Phonon Thermal Conductivity of Fine-Grained Undoped Lead Telluride, *Materials Transactions*, (2020). [doi:10.2320/matertrans.MT-M2020069].